https://doi.org/10.5194/egusphere-2026-1541
Preprint. Discussion started: 6 May 2026

Impact of sea ice rheological parameters and grounded iceberg distribution on Antarctic landfast sea ice: a sensitivity study with CICE version 6.4.1

Daniel P. Atwater[1,2,3], Pat Wongpan[1,2,4], Siobhan O'Farrell[5,6], Will Hobbs[1,2], Paul Spence[1,2,7,8], Mathieu Plante[9], Jean–François Lemieux[9], Alexander C. Bradley[10], Caitlin Adams[10], and Alexander D. Fraser[1,2]

[1]Institute for Marine and Antarctic Studies, University of Tasmania, Hobart, Tasmania Australia
[2]Australian Antarctic Program Partnership, Institute for Marine and Antarctic Studies, University of Tasmania, Hobart, Tasmania Australia
[3]Australian Defence Force, Canberra, Australian Capital Territory
[4]Australian Antarctic Division, Department of Climate Change, Energy, the Environment and Water, Kingston, Tasmania, Australia
[5]CSIRO Environment, Aspendale, Victoria, Australia
[6]University of Melbourne, School of Mathematics and Statistics, Melbourne, Australia
[7]Australian Centre for Excellence in Antarctic Science, Hobart, Tasmania, Australia
[8]Australian Centre of Excellence for 21st Century Weather, University of Tasmania, Hobart, Tasmania, Australia
[9]Recherche en Prévision Numérique Environnementale, Environnement et Changement Climatique Canada, Dorval, QC, Canada
[10]Geoscience Australia, Symonston, ACT 2601, Australia

Correspondence: D. P. Atwater (daniel.atwater@utas.edu.au)

Abstract. Landfast sea ice (fast ice) is a prominent feature of the Antarctic coastal environment. It plays key roles as a climate driver in the hydrological dynamics of the Antarctic continental shelf and serves as a critical habitat. However, despite its importance, Antarctic fast ice remains poorly represented in most global climate models. This study addresses key knowledge gaps in sea–ice modelling for realistically simulating Antarctic fast ice within an elastic–viscous–plastic rheological framework using a stand–alone sea–ice model. We conduct a suite of pan–Antarctic $1/4^{\circ}$ stand–alone sea–ice model simulations to quantify the role of grounded icebergs and to systematically test the influence of key rheological parameters (yield–curve ellipse aspect ratio, tensile strength, and ice strength) in sustaining fast ice. To support this, we introduce a new grounded iceberg dataset and a method to prescribe realistic grounded iceberg distributions based on observations. Our results show that the model reproduces the observed spatial distribution, seasonal maximum, and growth and retreat rates of Antarctic fast ice. Simulated fast ice reproduces the observed seasonal climatology but captures only limited inter–annual variability in circum–Antarctic fast–ice area. We demonstrate that simulated fast ice is highly sensitive to the ellipse aspect ratio (controlling the shear strength of the yield curve), tensile strength magnitude, and the presence and distribution of grounded icebergs. Realistic Antarctic fast ice is produced with an ellipse aspect ratio of 1.2, a tensile strength of 0.2, and a prescribed pan–Antarctic grounded iceberg extent of ~ 580 grid cells distributed consistently with observations. In this configuration, comparison with an otherwise similar simulation without grounded icebergs indicates that approximately 83% of simulated fast–ice area de-

https://doi.org/10.5194/egusphere-2026-1541
Preprint. Discussion started: 6 May 2026

pends on grounded icebergs as mechanical anchoring points. Importantly, these rheology and grounded iceberg modifications do not degrade the simulation of overall sea–ice area, thickness, or velocity in the Southern Ocean in our stand–alone simulations. These findings provide practical guidance for improving Antarctic fast–ice representation in coupled climate models through realistic grounded iceberg representation and targeted tuning of rheological parameters.

1 Introduction

Landfast sea ice (LFI) is immobile sea ice that is anchored to stable geographic features, such as the seabed, coastline, ice shelves, or grounded icebergs (GIBs). Sea ice is generally classified as landfast if immobilised for longer than some threshold time period—typically 15-20 days (Mahoney et al., 2007b, 2014; Fraser et al., 2020). Around Antarctica, LFI is observed on most of the coastline during any given year (Fraser et al., 2021). While some Antarctic LFI persists over multiple summer seasons (termed "multi–year LFI"), the majority—approximately two–thirds—is seasonal (Fraser et al., 2021). It generally reaches its maximum extent ($\sim 601 \times 10^3\,\mathrm{km}^2$) in October and its minimum extent ($221 \times 10^3\,\mathrm{km}^2$) in March (Fraser et al., 2021). Antarctic LFI is a key component of the sea ice–ocean interface, playing a multifaceted role in shaping both physical processes and ecological systems. It provides essential habitats for iconic species such as emperor penguins (*Aptenodytes forsteri*) (Aptenodytes forsteri; Labrousse et al., 2021) and Weddell seals (*Leptonychotes weddellii*) (Ainley et al., 2015), and contributes to the mechanical stability of ice shelves and glacier tongues by damping ocean swell and tidal energy (Massom et al., 2018; Teder et al., 2022). Importantly, persistent LFI is not evenly distributed, with multi–year LFI found within Lützow–Holm Bay, in the western part of Prydz Bay, Sulzberger Ice Shelf, and Shackleton Ice Shelf, where GIBs and coastal geometry (Porter-Smith et al., 2021) act together to promote stability.

The physical characteristics of LFI are shaped by a combination of mechanical and thermodynamic processes (Mahoney et al., 2014). Mechanically, LFI can form through the convergence of mobile sea–ice floes, which become arrested against coastal or grounded features and gradually consolidate into a stationary ice mass (Mahoney et al., 2007b). This dynamically–formed LFI typically exhibits a rough, deformed surface, particularly near its seaward margin, where repeated collisions and pressure ridging dominate (Mahoney et al., 2007b; Lange et al., 2025). In contrast, thermodynamic processes generate smoother, more uniform LFI through the in–situ freezing of seawater during quiescent conditions. Such thermodynamically–formed LFI is common in sheltered embayments or behind coastal promontories, where reduced mechanical interaction allows ice to freeze and consolidate steadily (Giles et al., 2008). The relative contributions of these two formation modes determine the morphology, structural integrity, and seasonal persistence of LFI across the Antarctic margin (Wongpan et al., 2025). This duality is also reflected geographically: for example, thermodynamically–formed LFI dominates embayments such as McMurdo Sound and Marguerite Bay, whereas mechanically–formed LFI features more prominently along exposed margins of East Antarctica (Maksym et al., 2012; Inall et al., 2022).

In Antarctica, the bathymetry of the continental shelf facilitates the grounding of icebergs along many coastal margins (Massom et al., 2001), where they act as physical anchor points that mechanically couple sea ice to the grounded iceberg and directly enable the formation and long–term persistence of LFI (Wright and Priestly, 1922; Kusahara et al., 2010; Nakayama

https://doi.org/10.5194/egusphere-2026-1541
Preprint. Discussion started: 6 May 2026

et al., 2014). This grounding typically occurs in waters shallower than 500 m (Fraser et al., 2023). This differs from Arctic LFI which typically depends upon sea ice keels grounding at water depths less than 30 m (Mahoney et al., 2007a; Lemieux et al., 2015, 2016). Fraser et al. (2021) showed that the persistence–weighted mean bathymetric depth associated with LFI is ∼403 m and noted that the ∼400 m isobath provides only a region–dependent, first–order indicator of persistent LFI. In addition to GIBs, coastline geometry (embayment/protrusion complexity and aspect) can promote or inhibit Antarctic LFI by providing sheltered embayments that favour thermodynamic growth and by enabling interception of drifting pack ice by coastal protrusions (Porter-Smith et al., 2021).

Both first–LFI and Multi–year LFI can exert a buttressing effect on adjacent ice shelves and glacier tongues by restraining seaward motion and, in some settings, reducing calving rates (Gomez-Fell et al., 2022). This mechanical coupling provides one motivation for improving the representation of LFI in numerical models, particularly in regions where persistent nearshore ice modifies the stress regime acting on floating ice and ice tongues.

Separately, LFI plays an important role in Antarctic coastal polynyas by defining a stable coastal boundary that interacts with offshore winds and geometry to regulate polynya location and extent (Nihashi and Ohshima, 2015; Fraser et al., 2019). Observations show that LFI can enhance polynya size and total sea ice production by deflecting consolidated pack ice away from the coastline, but can also suppress sea ice production when extensive LFI coverage masks active ice–growth areas (Fraser et al., 2019). Because polynyas are key sites of brine rejection, these LFI—polynya interactions influence dense shelf water formation and downstream contributions to Antarctic bottom water (Orsi et al., 2001; Morales Maqueda et al., 2004; Johnson, 2008; Tamura et al., 2016; Pirlet et al., 2025). Consequently, realistic simulation of LFI is relevant not only for coastal sea–ice distribution, but also for coupled oceanographic impacts mediated through polynya activity (Kusahara et al., 2017b; Cougnon et al., 2017; Van Achter et al., 2022).

Antarctic LFI also influences ecosystem processes: it provides an important habitat for ice–algal growth (Wongpan et al., 2024), and its seasonal development regulates light, stratification, and nutrient supply in adjacent coastal waters, with marked effects documented in regions such as Prydz Bay and the Ross Sea (Henley et al., 2023). In this way, LFI links the physical sea–ice environment to coastal biogeochemistry and food–web functioning (Fraser et al., 2023).

1.1 Modelling of Fast Ice

Modelling the formation and persistence of LFI has relied on various parameterisations. In a study of Arctic LFI, Lieser (2004) introduced a heuristic scheme based on sea–ice thickness, distance to a coastline, and ocean depth. In essence, grid cells sufficiently close to the coast were declared LFI once the ice thickened to a prescribed threshold relative to local bathymetry (as a proxy for keel grounding), and the ice velocity was then set to zero until thermodynamic melt reduced thickness below the threshold, at which point the ice could again advect. Their model successfully reproduced observed coastal polynyas and adjacent LFI in the Laptev Sea. However, because the LFI state is imposed diagnostically (i.e., by prescribing immobility once a geometric/thickness condition is met) rather than emerging from the modelled stress balance, the approach cannot represent mechanically–driven detachment events or the persistence of LFI in regions where stability depends on internal stress transmission (e.g., arching and resistance to fracture under wind– and current–driven forcing). More generally, prognostic

https://doi.org/10.5194/egusphere-2026-1541
Preprint. Discussion started: 6 May 2026

LFI requires a stabilising mechanism in the momentum balance that can resist divergence and maintain arches; in standard viscous–plastic formulations without an explicit tensile component, the ice offers little or no resistance to tensile stresses so confined or anchored ice can readily fracture and detach unless additional physics (e.g., tensile strength or an equivalent drag/anchoring parameterisation) is included (e.g., Hibler, 1979; König-Beatty and Holland, 2010; Lemieux et al., 2016).

A key step toward prognostic LFI in coupled models was to introduce a seabed stress into the sea ice momentum equation. Lemieux et al. (2015) proposed a bathymetry–dependent seabed stress term (τ_b) to represent resistance associated with keel grounding in shallow water, thereby suppressing drift and enabling LFI to form and persist along Arctic coasts. In a subsequent circum–Arctic evaluation, Lemieux et al. (2016) showed that LFI extent and persistence are strongly sensitive to the inclusion and magnitude of tensile strength parameter ($\mathrm{k_T}$) and to the ellipse aspect ratio of the yield–curve (e). These results highlight that realistic simulated LFI requires both an anchoring mechanism and sufficient shear and tensile strengths to form sea ice arches (e.g., Hibler, 1979; König-Beatty and Holland, 2010; Lemieux et al., 2016).

However, the seabed stress mechanism introduced to represent *sea–ice keel* grounding in shallow water is expected to have a limited impact in Antarctic applications, because direct keel–seabed interaction is confined to a very small number nearshore areas there. Whereas shallow Arctic shelves (often < 20 m) permit frequent ice–seafloor interaction, the Antarctic continental shelf is typically much deeper—commonly exceeding 300-$500\,\mathrm{m}$—and the "coastline" is often defined by steep ice–shelf fronts rather than gently sloping shores. This greatly limits *sea ice keel* grounding to small nearshore zones, while deep troughs and complex ice–shelf margins further complicate any simple grounding criterion (Porter-Smith et al., 2021). Consequently, Antarctic LFI requires alternative stabilising mechanisms, including physical pinning by GIBs and/or lateral drag at fixed boundaries (coastlines and ice–shelf fronts). Lateral drag parameterisations have also been proposed as a complementary stabilising mechanism for Arctic LFI in deep marginal seas (Liu et al., 2022). In this study, we focus on the former by developing a new circum–Antarctic GIB dataset and testing its impact in a controlled modelling framework (Section 2).

1.2 Previous Antarctic Fast Ice Modelling Studies

Several Antarctic modelling studies have examined coastal ocean–ice interactions with LFI prescribed as a static boundary condition based on observational LFI distributions. In these studies (e.g., Cougnon et al. (2013); Gwyther et al. (2014); Kusahara et al. (2017a); Cougnon et al. (2017), and Xia et al. (2023)), LFI is implemented as a fixed structure with minimal or no evolution in space or time. For example, Kusahara et al. (2017a) represented LFI as a thin ice–shelf–like barrier of uniform thickness ($15\,\mathrm{m}$) to investigate dense shelf water formation along Adélie and George V Lands, while Cougnon et al. (2017) and Xia et al. (2023) used prescribed LFI to examine sea–ice–ocean coupling and eddy–tide interactions in East Antarctica. Such idealised prescriptions provide stable boundary conditions that can be useful for isolating hydrographic responses, but they cannot represent the observed spatial and temporal variability of LFI formation and retreat, and they do not allow LFI to respond dynamically to forcing.

Fully prognostic Antarctic LFI simulations have only recently been demonstrated in regional coupled–model studies. Huot et al. (2021) showed that LFI can emerge in a fully coupled ocean–sea ice–atmosphere simulation of the East Antarctic coastal zone when the rheology includes tensile strength and stabilising anchors are present in the form of grid cells modified to

https://doi.org/10.5194/egusphere-2026-1541
Preprint. Discussion started: 6 May 2026

represent grounded icebergs. Their experiments reproduced key spatial and seasonal characteristics of LFI in Adélie Land and highlighted the importance of both rheological support and grounded constraints for maintaining attachment under realistic forcing. Similarly, in a high–resolution regional coupled configuration centred on the Totten Ice Shelf (Totten Ice Shelf), Van Achter et al. (2022) found that regional LFI formation required prescribed GIBs represented as land–masked grid cells derived from the RADARSAT–1 Antarctic Mapping Project Synthetic Aperture Radar (SAR) mosaic (September–October 1997; Jezek et al. 2013). Because this period coincides with peak LFI extent in the region (Fraser et al., 2021), distinguishing GIBs from seasonally immobilised ice can be challenging; Van Achter et al. (2022) addressed this using a cumulative iceberg–area threshold and a depth criterion (grounding proxy in water shallower than $450\,\mathrm{m}$). Together, these regional studies demonstrate that Antarctic LFI can be simulated prognostically in coupled systems, but they remain geographically limited and do not yet provide a circum–Antarctic assessment of LFI controls.

At the pan–Antarctic scale, Pirlet et al. (2025) implemented a circumpolar representation of LFI in NEMO–SI3 by restoring sea ice velocity toward zero within the spatial and temporal bounds of Fraser et al. (2020) observational Antarctic fast ice dataset (F2020). Their hindcast simulations (2001–2017) showed that constraining LFI in this way improves the realism of simulated coastal polynyas, LFI thickness, and summer sea ice extent, and provided a first pan–Antarctic estimate of LFI volume ($\sim$10.6% of total sea ice volume). However, because the method imposes LFI through an observational mask, it does not allow tests of the physical mechanisms that generate and maintain LFI, nor does it readily generalise to periods outside the observational record. This reinforces the need for prognostic Antarctic LFI capability in sea–ice and coupled ice–ocean models.

1.3 Study Objectives

Recent Antarctic–focused regional modelling studies demonstrate that prognostic LFI is achievable when stabilising mechanisms are represented (e.g., Huot et al., 2021; Van Achter et al., 2022). Here we extend this to a circum–Antarctic setting for the first time, and quantify the sensitivity of simulated LFI to key rheological parameters and prescribed GIBs. Since the Huot et al. (2021) and Van Achter et al. (2022) models rely on rheological formulations to simulate LFI, a systematic investigation of parameter sensitivity is essential to extending these approaches across the broader Southern Ocean domain. While these important rheological parameters (e.g., tensile strength, ellipse aspect ratio) have been studied in Arctic contexts, their influence on LFI in the Antarctic remains poorly constrained.

The present study advances our understanding of Antarctic LFI by testing whether a realistic simulation can be achieved in a stand–alone sea–ice model, with the aim of informing parameter choices governing LFI representation in climate models. We achieve this through a series of targeted sensitivity experiments on key rheological parameters and by prescribing various GIBs fields. Firstly, we assess the skill in maintaining realistic overall Antarctic sea ice area, thickness and drift velocity with LFI–specific parameterisations. Secondly, we introduce a new pan–Antarctic GIB dataset and evaluate the sensitivity of LFI simulation to the presence, concentration, and spatial distribution of GIBs. Thirdly, we identify which parameters exert strong control on resulting LFI extent and persistence. We focus on the rheological parameters $\mathrm{k_T}$ (König-Beatty and Holland, 2010) and e, together with the ice strength parameter ($\mathrm{P^*}$) and concentration scaling parameter ($\mathrm{C^*}$) (Hibler, 1979), and the

https://doi.org/10.5194/egusphere-2026-1541
Preprint. Discussion started: 6 May 2026

Elastic–Viscous–Plastic rheology (EVP) subcycling parameter N_{dte} (Hunke and Dukowicz, 1997) which controls the number of sub–cycles per time–step. To characterise variability beyond the core sensitivity period, we also extend two representative configurations over a 30–year span, enabling assessment of spatial patterns, the timing and magnitude of seasonal maxima and minima, and inter–annual variability of circum–Antarctic LFI. These three objectives collectively support a broader effort to inform targeted improvements in coupled climate models through refined representation of LFI in the Southern Ocean as an inherent constituent of modelling sea ice (Vancoppenolle et al., 2025).

2 Datasets and Methods

2.1 Circum–Antarctic Sub–Grid–Scale Grounded Iceberg Dataset

Previous studies have incorporated GIBs into Antarctic sea ice models by prescribing them in static land–mask grid cells. In their regional simulations, Huot et al. (2021) manually digitised iceberg locations from LANDSAT imagery (2011–2015), representing them as fixed land points in the sea ice and surface flux modules. Similarly, Van Achter et al. (2022) derived their GIB mask from the RADARSAT–1 Antarctic Mapping Mission SAR mosaic acquired in September–October 1997 (Jezek et al., 2013). Grid cells were flagged as GIBs (i.e., represented as isolated islands) if the cumulative iceberg area within a cell exceeded $2\,\mathrm{km}^2$, provided the local bathymetry was shallower than $450\,\mathrm{m}$ (Huot et al., 2021). Both studies relied on manual classification of a limited number of regional GIBs, and until our current work, presented here, no contemporary circum–Antarctic GIB dataset existed that could be directly mapped to climate–model grids.

To address this gap, we construct a new circum–Antarctic GIB dataset from March 2024 SAR imagery and distribute it alongside this work. The dataset targets icebergs that remain stationary during late summer, when LFI is close to its seasonal minimum (Fraser et al., 2021), thereby maximising the likelihood that detected stationary features correspond to grounded (rather than temporarily fastened) icebergs. The construction workflow and quality–control procedures are summarised here and described in detail in Appendix A. A limitation of any late–summer snapshot is that residual LFI or episodic pack–ice convergence (sea–ice compressed locally by winds/currents against the coast or other obstacles) can temporarily immobilise icebergs, potentially introducing false positives. We expect this effect to be further reduced in 2024 because Antarctic sea–ice extent remained exceptionally low (the second lowest year on record) through both the February minimum and the winter maximum, indicating unusually open coastal–ice conditions overall (Abram et al., 2025).

We follow Huot et al. (2021) and Van Achter et al. (2022) by representing GIBs as static “islands” (i.e., land–mask grid cells) within the sea–ice model. Directly incorporating every detected iceberg using this approach would require extensive landmask modification, producing unrealistic false promontories and artificial coastal barriers. In coupled configurations, such barriers would also be expected to disrupt ocean circulation, while simultaneously leaving too few ocean grid cells available to sustain realistic LFI development. To manage this, as with Huot et al. (2021) and Van Achter et al. (2022), we do not modify the grid for every single grounded iceberg in the dataset. Instead, we apply a probability–weighted thinning algorithm that reduces the number of GIB cells implemented as land–mask “islands” while preserving large–scale spatial density. We let c be the observed iceberg count in a model grid cell; then we compute a retention probability $p(c)$ (Appendix A, Equation A1) and

https://doi.org/10.5194/egusphere-2026-1541
Preprint. Discussion started: 6 May 2026

retain the cell if $u < p(c)$ for $u \sim \mathcal{U}(0,1)$, with isolated cells deterministically retained (Appendix A). Each realisation therefore yields a different binary subset that is statistically consistent with observed GIB density. This probabilistic framework ensures consistency with observed spatial patterns while maintaining model realism. The thinned GIB dataset, hereafter referred to as grounded iceberg thinning parameter (GIB_θ), is implemented as a binary mask. Each realisation of GIB_θ selects a unique binary subset of GIBs accordingly. An additional advantage of this probabilistic approach is that multiple realisations of GIB_θ can be generated, providing a means to assess the robustness of model behaviour to different–but observationally consistent–GIB configurations.

As in Huot et al. (2021) and Van Achter et al. (2022), representing GIBs as "islands" overly simplifies their physical representation: each retained iceberg occupies an entire model grid cell, fully blocking all ocean exchange through that cell. This simplification is more pronounced in our case due to the coarser model resolution used in our (global) simulations, where individual grid cells south of $60°$S typically represent $\sim 60 - 200\,\mathrm{km}^2$ of ocean. While this approach does not permit iceberg–ocean interaction or partial cell permeability, its impact is less critical in our present study given that the focus here is on LFI sensitivity rather than ocean circulation or thermodynamic feedbacks. Indeed, this caveat reinforces the suitability of performing these sensitivity experiments in sea ice–only (stand–alone) mode, where landmask modifications do not interfere with coupled ocean processes.

Despite observational evidence that GIBs strongly influence LFI formation and extent around Antarctica (Massom et al., 1998; Fraser et al., 2021), GIBs have had limited incorporation into prognostic sea ice models, largely due to the historical absence of high–resolution, circum–Antarctic datasets detailing their distribution. Without a representation of GIBs, models struggle to reproduce the spatial structure and seasonal persistence of Antarctic LFI, particularly in regions lacking complex coastal geometry (Li et al., 2020a). The dataset and thinning approach introduced here address this gap and provide an observationally grounded pathway for prescribing GIBs in stand–alone sensitivity experiments.

2.2 CICE Stand–alone Configuration

We employ the Los Alamos Community sea Ice CodE version 6.4.1 (CICE) model (Hunke et al., 2022) in stand–alone mode, driven by prescribed atmospheric and oceanic forcing fields. This configuration CICE (version 6.4.1) stand–alone configuration (i.e. without a coupled ocean model) (CICE6–SA) omits interactive ocean–sea ice feedbacks, but provides a computationally efficient framework for controlled experimentation on sea ice processes. By holding the oceanic and atmospheric drivers fixed, the stand–alone configuration enables systematic sensitivity testing of rheological parameters and model configurations over extended simulation periods. This approach allows us to isolate the dynamic controls on Antarctic LFI and evaluate how key parameters influence its simulated extent and variability. This approach prioritises understanding the physical process—particularly of mechanical interactions and GIB constraints—over detailed thermodynamic coupling with the ocean. Our model setup is similar to that of Day et al. (2024), who similarly focused on dynamic processes in CICE, while using prescribed or restored boundary conditions.

The model domain uses the global Australian Community Climate Earth–System Simulator at $1/4°$ horizontal resolution (ACCESS–OM2–025) tri–polar Arakawa–B grid from Kiss et al. (2020). Simulations span 1 January 1993 to 31 December

https://doi.org/10.5194/egusphere-2026-1541
Preprint. Discussion started: 6 May 2026

1999, with two extended runs continuing to 31 December 2023. Daily outputs include key diagnostic fields such as ice concentration (a_{ice}), thickness (h_{ice}), velocity components (u_{ice}, v_{ice}), internal strength and stresses, and thermodynamic fluxes. Sea ice dynamics are governed by the EVP rheology, with a base thermodynamic time step of $\Delta t = 1800$s. Subcycling within EVP is managed through two nested loops: the dynamic–thermodynamic coupling time step is subcycled once per Δt, and the internal EVP solver performs $N_{\mathrm{dte}} = 240$ iterations to resolve the stress–strain relationship. This value reflects a balance between computational efficiency and numerical stability (Kimmritz et al., 2016). Most experiments in this study employ the revised EVP formulation from Bouillon et al. (2013), which improved the spatial realism of simulated Antarctic sea ice cover in preliminary tests. Sea ice thermodynamics are represented using the mushy–layer conductive scheme with five thickness categories. Ice internal stresses are computed with the standard EVP elliptical yield–curve (e), which controls the relative resistance to shear versus compression—decreasing e increases the effective shear strength. All simulations are initialised with no sea ice cover, and daily–averaged history files are generated throughout. Simulation settings are summarised in Table 1.

Atmospheric forcing is taken from the European Commission on Medium–range Weather Forecasting (ECMWF) Reanalysis version 5 (ERA5) dataset (Hersbach et al., 2020), and includes hourly fields of 10 m wind vector components (u_{10}, v_{10}), 2 m air and dew–point temperatures, surface pressure, downward short–wave and long–wave radiation, and total precipitation. To map ERA5 fields onto the model grid, we perform bilinear remapping using the Earth System Modeling Framework (ESMF) library (Hill et al., 2004; Zhuang et al., 2021) with nearest–neighbour extrapolation. The forcing routine is handled within the custom CICE6–SA Fortran module that reads, masks, and interpolates two temporal snapshots of the forcing fields, using the local interpolation coefficients `c1intp` and `c2intp` to compute an hourly temporally–weighted state $f(t) = c_1 f(t_0) + c_2 f(t_1)$, where $f(t_0)$ and $f(t_1)$ are forcing snapshots bracketing the current model time, and $c_1 + c_2 = 0.5$, which is based on the model time–step (Δt).

Sea Surface Temperature (SST), salinity, and ocean surface velocity components are prescribed from the ECMWF Ocean Reanalysis System version 5 (ORAS) ocean reanalysis product (Zuo et al., 2019). These fields are re–gridded to the model grid using bilinear interpolation with nearest–neighbour extrapolation (via ESMF), and are stored without depth–averaging prior to being used as forcing inputs. Temporal interpolation is applied in the same manner as for the atmospheric forcing.

A key feature of our CICE6–SA configuration is the implementation of a daily SST restoring mechanism. This nudging approach constrains the model–predicted sea surface temperature to remain close to the observed SST, thereby maintaining consistent thermodynamic gradients at the ice–ocean interface and supporting realistic surface energy fluxes. Following the formulation of Day et al. (2024), the restoring is applied at every timestep using:

$$\mathrm{SST}_{\mathrm{new}} = \mathrm{SST}_{\mathrm{model}} + \frac{\Delta t}{t_{\mathrm{rest}}} \left(\mathrm{SST}_{\mathrm{obs}} - \mathrm{SST}_{\mathrm{model}}\right) \tag{1}$$

where Δt is the model timestep and t_{rest} is the restoring timescale. In this study, we set `trestore` = 1 day to achieve daily nudging toward the prescribed SST field.

In addition to SST restoring, other oceanic forcing fields are treated to ensure numerical stability and physical realism. Sea surface salinity is constrained within a physically realistic range (5-47 PSU) to prevent numerical artefacts, and ocean surface currents from ORAS are filtered to remove anomalous spikes. The CICE6–SA configuration employs the internal

https://doi.org/10.5194/egusphere-2026-1541
Preprint. Discussion started: 6 May 2026

mixed–layer formulation in CICE, with a fixed mixed–layer depth set to $60\,\mathrm{m}$. This depth is consistent with observed climatological estimates of the Antarctic winter mixed layer, which typically range between 50-$70\,\mathrm{m}$ across much of the Southern Ocean (Petty et al., 2014; Pauling et al., 2016; Pellichero et al., 2017). While highly simplified compared to prognostic ocean models, prescribing a representative climatological depth avoids spurious thermodynamic behaviour in the absence of fully coupled ocean feedbacks, and provides a reproducible framework for isolating the sea ice rheological sensitivities of interest here.

The study period of 1993–1999 of most model runs was chosen to align with existing ACCESS–OM2–025 simulations, ensuring consistency with prior experiments and comparability across model configurations. Importantly, while the present configuration is an uncoupled sea ice model, it inherits many structural elements from the ACCESS–OM2–025 framework—including the tri–polar grid. In this sense, the CICE6–SA experiments occupy a hybrid space: they isolate ice physics from ocean feedbacks but remain closely aligned with the CICE configuration in ACCESS–OM2–025. This continuity ensures direct comparability with fully coupled ACCESS–OM2–025 simulations forced with ERA5, situating our stand–alone experiments within the broader ACCESS–OM2–025 modelling framework.

2.3 Table of Simulations

The full suite of experiments includes 26 sensitivity simulations, each varying a single parameter related to rheology and GIB configuration. We focus on rheological parameters that control the shape and strength of the yield curve and the ability of the ice pack to resist opening and shear: the ellipse aspect ratio (e), which defines the shear strength; the tensile strength factor ($\mathrm{k_T}$), which modulates resistance to tensile stresses; the ice strength parameter ($\mathrm{P^*}$) and its concentration scaling ($\mathrm{C^*}$); and, separately, the GIB concentration fraction (GIB_θ). The ranges sampled for each parameter (e.g., $\mathrm{e}=0.8$ to 2.5, $\mathrm{k_T}=0$ to 0.6, $\mathrm{P^*}=1\times10^4$ to 5×10^4, $\mathrm{C^*}=10$ to 30, and $\mathrm{GIB}_\theta=15$ to 35%) combine values previously shown to support realistic LFI behaviour in regional and global sea–ice models (e.g., Hunke (2001); Tremblay and Hakakian (2006); Dumont et al. (2009); König-Beatty and Holland (2010); Lemieux et al. (2016); Bouchat and Tremblay (2017); Toyota and Kimura (2018)) with additional exploratory tuning using CICE6–SA. Table 1 summarises all experiments, including parameter values and acronyms used throughout this paper.

2.4 Fast Ice Classification in Model Output

To evaluate modelled LFI, we apply two complementary classification methods to discriminate between drifting pack and stationary LFI: (**a**) a two–week "*rolling–mean*" approach; and (**b**) a "*binary–days*" persistence method. In previous modelling studies of LFI (Lemieux et al., 2015; Olason, 2016; Huot et al., 2021; Van Achter et al., 2022), the *rolling–mean* approach has typically been implemented using threshold–based criteria. Most notably, Lemieux et al. (2015) classify ice as LFI when two–week–averaged sea ice speed is below a fixed threshold of $5\times10^{-4}\,\mathrm{m/s}$ (corresponding to a sea ice displacement of $\sim660\,\mathrm{m}$ over two weeks). We employ a two–week rolling mean of sea–ice speed used distinguish LFI from pack ice (*rolling–mean*) method and classify a grid cell as LFI if it has sea ice concentration $>15\%$ and meets this average speed criterion. This produces a *rolling mean–based* LFI–*mask*, that we denote as $\mathcal{M}_{\mathrm{FI\_roll}}$.

https://doi.org/10.5194/egusphere-2026-1541
Preprint. Discussion started: 6 May 2026

Table 1. Summary of CICE6–SA sensitivity simulations and configuration parameters. Rows are grouped into: (i) forcing and GIB distribution experiments (`ry93` to `gi-mid-gi3`); (ii) ice–strength concentration–scaling experiments; (iii) ice–strength amplitude experiments; (iv) tensile–strength experiments; (v) yield–curve ellipse aspect–ratio experiments; and (vi) the combined "fast–ice favourable" configuration (`FI-heavy`). Unless otherwise stated, the default CICE6–SA configuration is `gi-mid` as follows: ellipse aspect ratio (e)= 2.0, tensile strength parameter (k_T)= 0.2, ice strength parameter (P^*)= 2.75×10^4, concentration scaling parameter (C^*)= 20, N_{dte} = 240, revised EVP enabled, and GIB_θ= 25%. The `elps-min` run (bold) is used as the primary fast–ice–representative experiment throughout. Simulations `gi-mid-gi1`, `gi-mid-gi2`, and `gi-mid-gi3` use identical rheological settings to `gi-mid`, but are run with different stochastic realisations of GIB placement to assess sensitivity to iceberg distribution. `notens-nogi` is the nearest equivalency to ACCESS–OM2–025 as can be achieved in CICE6–SA. `ry93` applies 1993 repeat–year atmospheric forcing (ERA5) to demonstrate CICE6–SA stability over the six–year period.

Run Name	Long Name	Brief Description
`ry93`	Repeat Year Forcing	1993 repeat–year forcing
`notens-nogi`	ACCESS–OM2–025 equivalent	No tensile strength, no GIBs (unmodified landmask), default e= 2.0
`gi-mid`	**Control run**	Mid–range concentration of GIBs with GIB_θ = 25%
`gi-max`	Grounded iceberg maximum	Highest concentration of GIBs with GIB_θ= 35%
`gi-min`	Grounded iceberg minimum	Lowest concentration of GIBs with GIB_θ= 15%
`gi-nil`	No grounded iceberg but landfast sea ice–enabled	Unmodified ACCESS–OM2–025 land–mask; favourable rheology for LFI with k_T= 0.3, e= 1.2, $P^* = 5\times10^4$, $C^* = 10$
`gi-nil-def`	No grounded iceberg, default rheology	Unmodified ACCESS–OM2–025 landmask with default CICE6–SA parameters
`gi-mid-gi1`	Grounded iceberg perturbation 1	Alternate randomised configuration of GIBs, GIB_θ= 0.25
`gi-mid-gi2`	Grounded iceberg perturbation 2	Alternate randomised configuration of GIBs, GIB_θ= 0.25
`gi-mid-gi3`	Grounded iceberg perturbation 3	Alternate randomised configuration of GIBs, GIB_θ= 0.25
`Cstar-max`	Concentration scaling parameter maximum	Strong strength decay with decreasing sea ice concentration, $C^* = 30$
`Cstar-min`	Concentration scaling parameter minimum	Weak strength decay with decreasing sea ice concentration, $C^* = 10$
`Pstar-max`	Ice strength parameter maximum	High ice strength, $P^* = 5\times10^4$
`Pstar-min`	Ice strength parameter minimum	Low ice strength, $P^* = 1\times10^4$
`ktens-nil`	Tensile strength parameter zero	Tensile parameterisation, disabled k_T= 0
`ktens-min`	Tensile strength parameter low	Low tensile strength, k_T= 0.10
`ktens-max`	Tensile strength parameter high	High tensile strength, k_T= 0.30
`ktens-ext`	Tensile strength parameter very high	Very high tensile strength, k_T= 0.60
`elps-max`	Ellipse aspect ratio very high	e= 2.5
`elps-mid`	Ellipse aspect ratio moderate	e= 1.6
`elps-ext`	Ellipse aspect ratio very low	e= 0.8
`elps-min`	Van Achter et al. (2022) configuration	e= 1.2
`FI-heavy`	Use of landfast sea ice favourable parameters from above	Same as `gi-nil` but with GIBs enabled; GIB_θ= 25%, k_T= 0.30, e= 1.2, $P^* = 5\times10^4$, $C^* = 10$

https://doi.org/10.5194/egusphere-2026-1541
Preprint. Discussion started: 6 May 2026

As a complement to this temporally–smoothed approach, we also implement a *binary–days* persistence classification. We additionally use a persistence–based diagnostic to test sensitivity to the temporal definition of "immobility" and to allow limited tolerance to short–lived mobility events, whereas the *rolling–mean* approach has been used in several modelling studies to characterise simulated LFI dynamics (e.g., Lemieux et al., 2015; Huot et al., 2021; Van Achter et al., 2022; Olason, 2016). Rather, we use a second diagnostic to test sensitivity to the temporal definition of "immobility" and to introduce controlled tolerance to short–lived mobility events. In particular, a strict two–week mean enforces persistence on the full window, whereas observed and simulated LFI can exhibit brief episodes of enhanced motion associated with storms, shear localisation, or partial break–up, followed by rapid re–fastening. The *binary–days* metric allows such transient excursions while still requiring sustained low–speed conditions on most days, thereby separating persistent fastening from intermittently mobile coastal ice. In this method, we apply the same concentration and speed thresholds to each daily–averaged simulation output to produce a *daily candidate* mask of low–mobility ice ("*daily–fast–ice*", denoted $\mathcal{M}_{\mathrm{FI\_day}}$). This field is used only as an intermediate diagnostic for the persistence filter below, and is not interpreted as LFI in the main results because instantaneous low speeds can occur in unconstrained pack ice during periods of weak forcing, yielding spurious LFI detections. Unless stated otherwise, all LFI area statistics and figures in the main text are computed from $\mathcal{M}_{\mathrm{FI\_bin}}$ rather than $\mathcal{M}_{\mathrm{FI\_day}}$. In the *binary–days* method, a grid cell is classified as persistently LFI at time t if it satisfies the daily thresholds on at least 9 of the past 11 days (Appendix B). This yields a LFI–persistence mask, $\mathcal{M}_{\mathrm{FI\_bin}}$, which reduces day–to–day intermittency in $\mathcal{M}_{\mathrm{FI\_day}}$ while retaining daily resolution for formation and breakup timing.

For all simulations in Table 1, we report circum–Antarctic LFI Area (FIA) as the pan–Antarctic sum of grid–cell area classified as LFI. In experiments that include GIBs, we add the total GIB footprint area (i.e. the cumulative sum of grid–cell area where the GIB mask is active) to the FIA, such that the reported value is $\mathrm{FIA_{tot}} = \mathrm{FIA_{FI}} + A_{\mathrm{GI}}$. This GIB contribution is a time–invariant offset on the model grid and is included in all experiments that prescribe a thinned GIB mask (i.e., all experiments except `notens-nogi`, `gi-nil`, and `gi-nil-def`). For reference, the total circum–Antarctic GIB area is approximately $6.7 \times 10^4\,\mathrm{km}^2$ for $\mathrm{GIB}_\theta = 25\%$ (used in all experiments other than those listed in the previous sentence), $3.8 \times 10^4\,\mathrm{km}^2$ for $\mathrm{GIB}_\theta = 15\%$ (`gi-min` experiment), and $1.48 \times 10^5\,\mathrm{km}^2$ for $\mathrm{GIB}_\theta = 35\%$ (`gi-max` experiment).

3 Results

3.1 Circum–Antarctic Validation of General Sea Ice Properties

To evaluate the realism of simulated sea ice in the Southern Ocean, we compare a set of CICE6–SA experiments with satellite–derived Sea Ice Area (SIA) observations from the United States National Snow and Ice Data Center (NSIDC) (Meier et al., 2021), and with two coupled ocean–sea ice models: ACCESS–OM2–025 (Kiss et al., 2020) forced with ERA5 and ORAS (Zuo et al., 2019). Three CICE6–SA experiments are provided here: `notens-nogi`, representing a default (unmodified to support fast ice) rheology without GIBs; `elps-min`, a fast–ice–favourable configuration (reduced $e = 1.2$, non–zero $k_T = 0.2$, and prescribed GIBs); and `ry93`, a repeat–year forcing experiment used solely to demonstrate numerical stability and isolate the impact of inter–annual forcing variability (with rheology otherwise close to the control), and `notens-nogi`

https://doi.org/10.5194/egusphere-2026-1541
Preprint. Discussion started: 6 May 2026

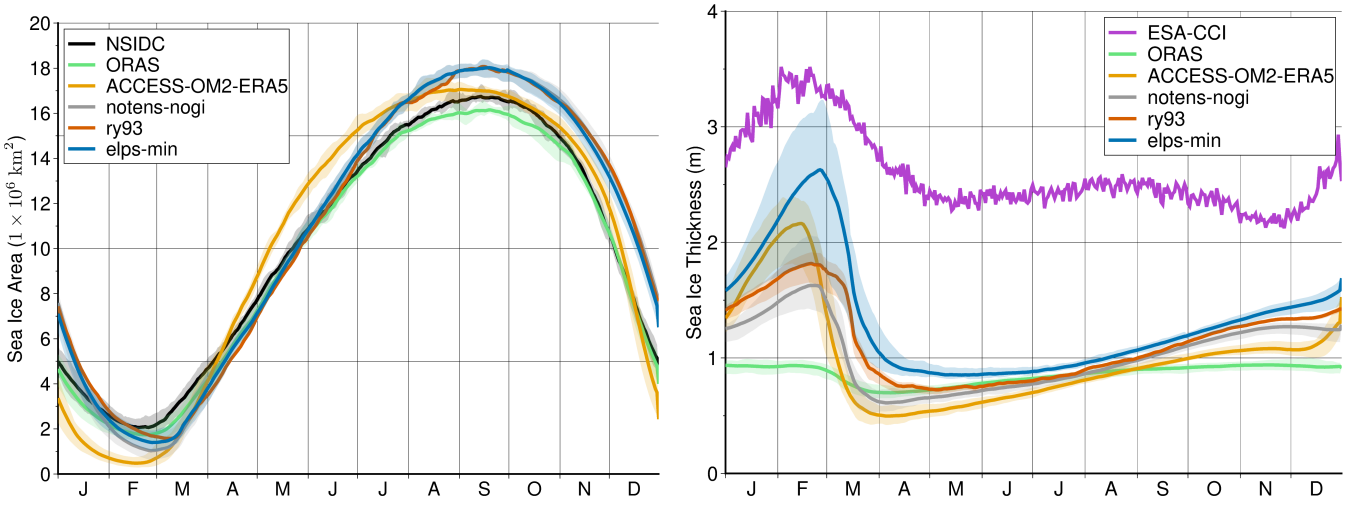

(a) Antarctic SIA climatology (1994–1999).

(b) Antarctic SIT climatology (models: 1994–2017; European Space Agency Climate Change Initiative (ESA–CCI): 2002–2017).

Figure 1. Circum–Antarctic validation of (a) Sea Ice Area (SIA) and (b) Sea Ice Thickness (SIT). Panel (a) shows mean daily climatologies (solid lines) of Antarctic SIA averaged over 1994–1999, with shaded bands denoting the inter–annual range for each model or observational product. Panel (b) shows the daily climatology of Antarctic SIT from model simulations (1994–1999) compared with the satellite–derived ESA–CCI climatology (2002–2017). In both panels, the legend distinguishes satellite observations (NSIDC in (a), ESA–CCI in (b)), CICE6–SA experiments (`notens-nogi`, `elps-min`, `ry93`), and coupled ocean–sea ice models (ACCESS–OM2–025, ORAS).

which has a very similar configuration to ACCESS–OM2–025. These three experiments are therefore best viewed as representative configurations—a "no–fast–ice" baseline (`notens-nogi`), a fast–ice–favourable tuned case (`elps-min`), and a repeat–year stability test (`ry93`)—rather than spanning the full range of pack–ice sensitivity sampled across the broader parameter ensemble. Together these runs sample the main parameter choices explored in this study while providing context for comparison against coupled systems. We first assess model skill in reproducing large–scale seasonal evolution of Antarctic SIA and Sea Ice Thickness (SIT) (Fig. 1), and then examine sea ice drift biases (Fig. 2).

Fig. 1a shows circum–Antarctic SIA climatologies averaged over 1994–1999. All CICE6–SA experiments capture the timing of the seasonal SIA maximum, while the minimum is shifted by (up to) a fortnight in some members. Relative to NSIDC observations and the coupled models, the CICE6–SA runs show slower early–season growth; during spring, the retreat begins from a larger SIA state (positive bias) and faster melt then narrows the gap into summer. This is likely due to the absence of ocean feedbacks such as mixed–layer heat fluxes and stratification, and to the prescribed ∼60 m mixed–layer depth used in the forcing, which largely sets the phase and amplitude of the pack–ice seasonal cycle (e.g., Petty et al., 2014). Among the CICE6–SA runs, inclusion of GIBs in `elps-min` modestly reduces the maximum SIA compared to `notens-nogi`, consistent with enhanced mechanical resistance, while `ry93` behaves similarly to `notens-nogi` but retreats slightly earlier due to year–specific forcing. All three CICE6–SA runs reach their maximum later in the year than ACCESS–OM2–025, aligning more closely with the observed October peak in NSIDC. These differences highlight both the benefits and trade–offs

https://doi.org/10.5194/egusphere-2026-1541
Preprint. Discussion started: 6 May 2026

of isolating sea ice physics: phasing is improved relative to the coupled system, but amplitude remains biased high without ocean–ice feedbacks.

To further evaluate the physical realism of simulated sea ice characteristics, the SIT climatologies in Fig. 1b compare the multi–year daily SIT cycle from each model with observational estimates from the ESA–CCI dataset (Hendricks et al., 2024). The ESA–CCI climatology, representing the 2002–2017 mean, provides a benchmark for evaluating model performance in the absence of direct *in situ* thickness measurements, because the ESA–CCI thickness product is derived primarily from radar–altimetry retrievals, it remains subject to larger uncertainties during the melt season and in coastal and marginal–ice zones (Trivedi et al., 2025). All simulations capture the strong seasonal cycle, with `elps-min` exhibiting the thickest ice, peaking at $\sim 2.6\,\mathrm{m}$ in late summer. However, all models underestimate Antarctic SIT relative to ESA–CCI, with late–summer biases of order 0.5–1 m and persistently thinner winter ice across the domain. The coupled ACCESS–OM2–025 simulation generally lies between the CICE6–SA experiments `elps-min` and `ry93`, consistent with ocean–ice feedbacks that limit thermodynamic thickening relative to the uncoupled configuration. The thicker late–summer ice in `elps-min` relative to `ry93` highlights sensitivity to the yield–curve ellipse aspect ratio: reducing e enhances shear resistance and promotes mechanical thickening via increased convergence and ridging (e.g., Dumont et al., 2009; Lemieux et al., 2016; Bouchat et al., 2022; Hutter et al., 2022). The `notens-nogi` and ACCESS–OM2–025 configurations share broadly similar rheological settings, so differences in their SIT maxima mainly reflect the impact of interactive ocean circulation and mixed–layer processes on ice growth and melt. In turn, the thicker late–summer ice in `elps-min` compared with `ry93` highlights the sensitivity of Antarctic SIT to the yield–curve ellipse ratio: reducing e from 2.0 to 1.2 enhances shear resistance and mechanical thickening, consistent with previous studies showing that smaller ellipse ratios increase ice–thickness (e.g., Dumont et al., 2009; Lemieux et al., 2016; Bouchat and Tremblay, 2017; Hutter et al., 2022). Taken together, these experiments suggest that the CICE6–SA framework produces a broadly realistic Antarctic SIT climatology, and systematically thicker ice than in the coupled and reanalysis systems, though still thinner than suggested by current satellite retrievals.

To assess the fidelity of simulated sea ice drift, Fig. 2 presents sea ice speed biases compared with satellite–derived sea ice drift from OSI–SAF (EUMETSAT, 2025) over the 1994–1999 period. The ice speed bias reveals that the coupled ACCESS–OM2–025 simulation exhibits a positive bias year–round–averaging $\sim 0.04\,\mathrm{m/s}$ over the winter months–indicating overly mobile sea ice. In contrast, `elps-min` and `notens-nogi` show more modest negative biases ($\sim 0.02\,\mathrm{m/s}$) during winter. ORAS speed differences relative to OSI–SAF are small (typically $< 0.01\,\mathrm{m/s}$), consistent with a reanalysis product in which sea–ice state is constrained by data assimilation and model dynamics.

Collectively, these metrics indicate that, relative to the coupled ACCESS–OM2–025 configuration (which exhibits overly mobile ice), the tuned CICE6–SA experiments—particularly `elps-min`—bring the representation of Antarctic sea ice dynamics closer to that implied by the NSIDC, ESA–CCI, and OSI–SAF observations, especially where the rheological parameters enable LFI growth.

https://doi.org/10.5194/egusphere-2026-1541
Preprint. Discussion started: 6 May 2026

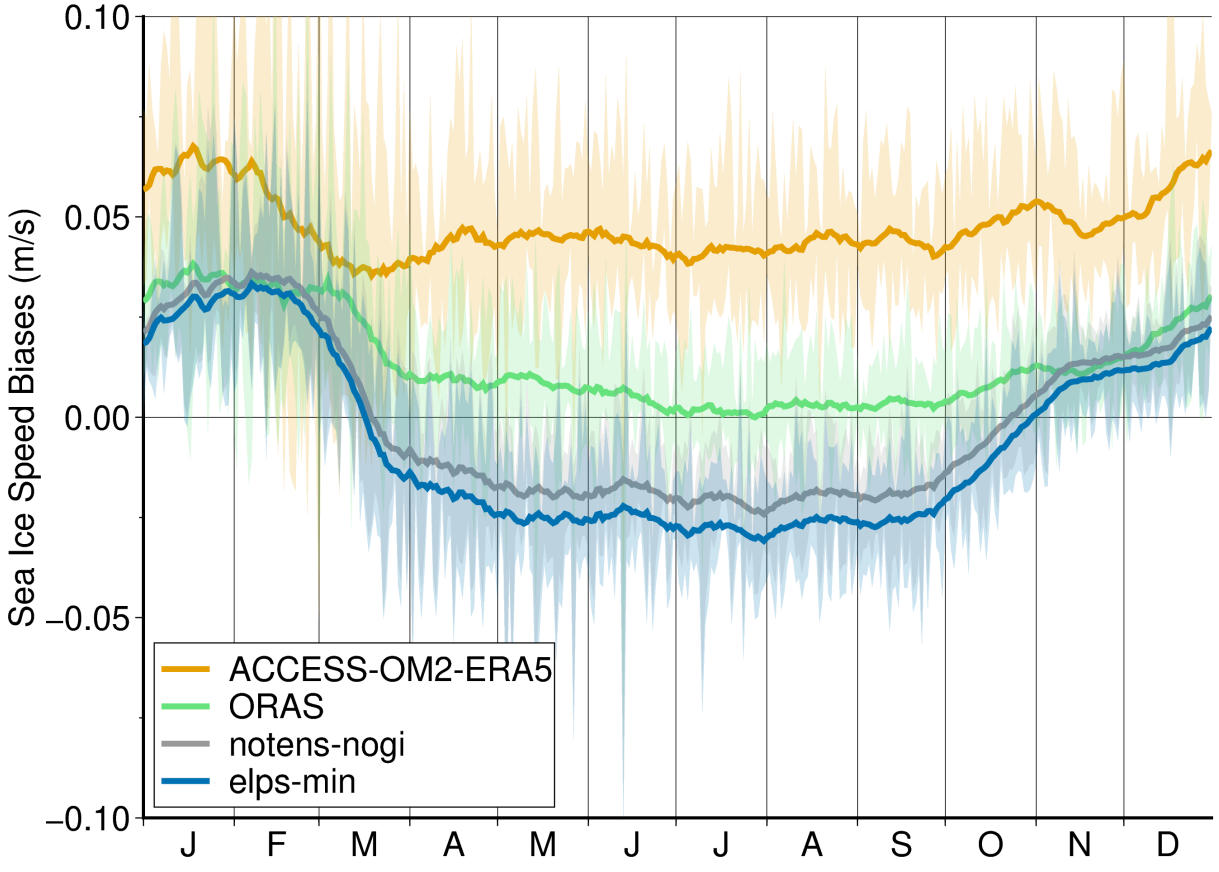

Figure 2. Climatological bias in Antarctic sea ice speed (m/s) for 1994–1999, calculated as model minus Ocean and Sea Ice Satellite Application Facility (OSI–SAF) satellite observations. Results are shown for two CICE6–SA configurations and for the coupled global models ACCESS–OM2–025 and ORAS. Shaded regions indicate inter–annual variability across the six–year climatology.

3.2 Parameter Modifications

Presenting and discussing LFI Persistence (FIP) as a map along with the time series of FIA allows for a discussion of both spatial distribution and seasonal cycle as is provided in this section. FIP, mapped in the lower panels of Figures 3–6, is the temporal fraction during which each grid cell satisfies the number of days daily fast ice was present out of over a given period of days used distinguish fast ice from pack ice (*binary–days*) classification criteria (see Section 2.4; orange line in these figures). To maintain legibility at circum–Antarctic scale, the persistence maps are shown as two longitudinal sectors that together span the major LFI regimes while avoiding excessive compression of the coastal band. The first sector (20°° W–160° E) covers much of East Antarctica, where slightly broader continental shelves support higher concentration of GIBs, contributing to more broad distribution of multi–year landfast sea ice (multi–year LFI) and contribute substantially to the circum–Antarctic FIA. The second sector (160°–20° W) includes the West Antarctic Peninsula and adjacent seas, where a highly indented coastline

https://doi.org/10.5194/egusphere-2026-1541
Preprint. Discussion started: 6 May 2026

(fjords, embayments, and island chains) promotes strong embayment anchoring, but less multi–year LFI and therefore provides a stringent test of whether the model captures persistence driven by small–scale coastal geometry. In combination, these sectors highlight whether parameter perturbations modify the persistence of LFI (spatial stability) rather than only the amplitude of the seasonal FIA cycle. Unless otherwise noted, results are presented using the *binary–days* classification, which we adopt as the primary diagnostic owing to its improved representation of persistent LFI (see Section 2).

To isolate the effect of mechanical anchoring and rheological resistance on simulated Antarctic sea ice, we first evaluate a baseline simulation—`notens-nogi`—configured as closely as possible to match the rheology parameters of ACCESS–OM2–025 (i.e., $k_T = 0.0$, $e = 2.0$, $P^* = 2.75 \times 10^4$, $C^* = 20$, and $GIB_\theta = 0$), without bathymetry modifications to simulate GIBs, or tensile strength. Hence `notens-nogi` serves here to assess the degree to which a typical rheology can generate and sustain LFI. Fig. 3 presents the resulting FIA and FIP from this `notens-nogi` simulation over 1994–1999. The top panel shows a comparison of fast ice climatology against the Fraser et al. (2020) observational Antarctic fast ice dataset. Both classification methods—*binary–days* and *rolling–mean* threshold—yield very low LFI extent throughout the year, peaking below $60 \times 10^3\ \mathrm{km}^2$ in July–August. In this baseline configuration, FIP is confined to sheltered deep embayments (e.g., McMurdo Sound; ∼165°E). This corresponds to less than one–tenth of the observed maximum $\sim(601.0 \times 10^3\ \mathrm{km}^2)$ and shows only very weak seasonality.

In Fig. 3 the few locations showing marginal LFI persistence are confined to the western Antarctic Peninsula, where geographic features such as fjords and narrow embayments offer natural protection from ice breakout. However, even in these regions, the persistence is low and discontinuous. These results confirm that in the absence of mechanical support from tensile strength or GIBs, the default sea ice rheology in CICE6–SA fails to produce the observed LFI distribution. This experiment establishes the necessity of enhanced rheological and anchoring mechanisms for realistic simulation of Antarctic LFI.

Next we introduce a moderate tensile strength into the rheology ($k_T = 0.2$; König-Beatty and Holland, 2010; Lemieux et al., 2016), while leaving other parameters unchanged (i.e. without the inclusion of GIBs). This configuration (`gi-nil-def`), shown in Fig. 4, also fails to reproduce LFI across most of the Antarctic coastline. Compared to the `notens-nogi` simulation (Fig. 3), the spatial distribution in `gi-nil-def` of FIP shows only very small improvements to pan–Antarctic LFI coverage, with near–zero LFI across much of Antarctica. The western Antarctic Peninsula remains the main region of simulated LFI, particularly within Marguerite Bay and adjacent inlets. This aligns with observations that complex fjord geometry and narrow inlets can restrict drift even in the absence of GIBs (Fraser et al., 2021), allowing LFI to persist through tensile strength alone. Elsewhere, CICE6–SA default rheology proves insufficient to immobilise ice. The seasonal cycle in the top panel of Fig. 4 shows a weakly–emerging seasonality of FIA, with the *binary–days* metric peaking very late (Nov–Dec timeframe) at just over $\sim 150 \times 10^3\ \mathrm{km}^2$—around one quarter of the observed maximum extent. Consistent with Huot et al. (2021) and Van Achter et al. (2022), the `gi-nil-def` experiment demonstrates that the addition of tensile strength alone cannot reproduce the observed magnitude or timing of Antarctic LFI.

To evaluate the impact of GIB anchoring on LFI formation, we next analyse a simulation identical in configuration to the previous experiment (moderate tensile strength, $k_T = 0.2$), but now prescribe some GIBs ($GIB_\theta = 25\%$) by reclassifying selected ocean grid cells as land (i.e., GIB "islands" in the landmask; see Section 2), thereby introducing fixed mechanical

https://doi.org/10.5194/egusphere-2026-1541
Preprint. Discussion started: 6 May 2026

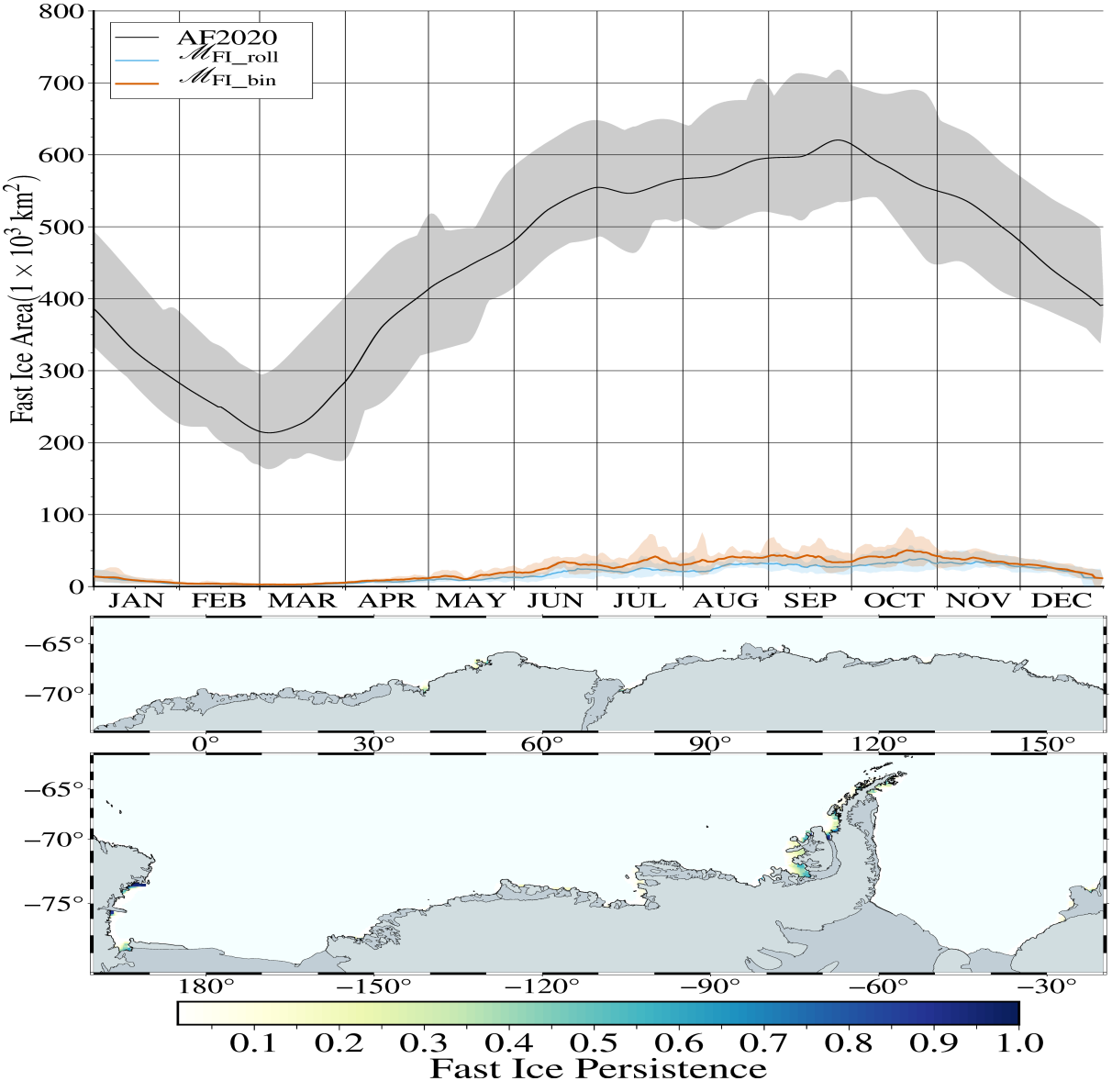

Figure 3. Circum–Antarctic LFI **area** (top) and LFI **persistence** (middle and bottom) over the period 1994–1999 from the CICE6–SA simulation `notens-nogi` without tensile strength or GIBs. **Top:** Daily climatology of total Antarctic LFI derived from *binary–days* ($\mathcal{M}_{\mathrm{FI\_bin}}$, orange), and *rolling–mean* ($\mathcal{M}_{\mathrm{FI\_roll}}$, cyan) classification schemes, against the F2020 observational LFI climatology (black) from Fraser et al. (2021). Shaded regions show the daily min/max climatology. **Middle and bottom:** Spatial distribution of LFI persistence (unitless fraction of days satisfying the *binary–days* criteria; 0 to 1). The persistence–based $\mathcal{M}_{\mathrm{FI\_bin}}$ diagnostic is used.

anchors in an experiment named `gi-mid`; with 583 GIB cells ($\sim 6 \times 10^4$ km^2). All other rheological and dynamic parameters remain unchanged from experiment `gi-nil-def`. This experiment enables a focused assessment of GIB–induced

https://doi.org/10.5194/egusphere-2026-1541
Preprint. Discussion started: 6 May 2026

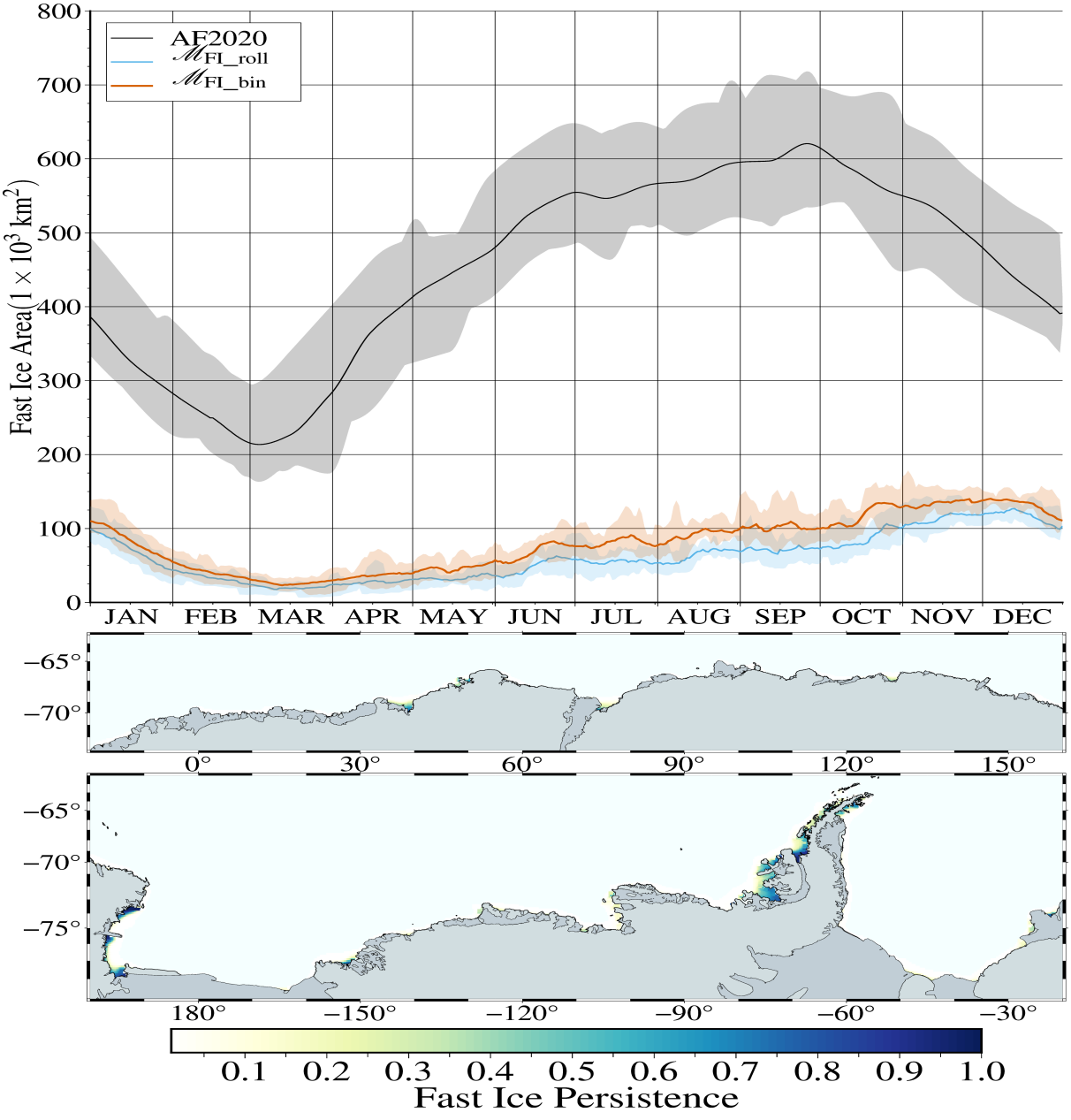

Figure 4. As in Fig. 3, but for the `gi-nil-def` simulation (tensile strength parameter= 0.2 and no GIBs). The orange line represents LFI from *binary–days* method which is also the LFI that is mapped in the two pan–Antarctic sub–panels.

mechanical stabilisation. The resulting FIA and FIP from this experiment are shown in Fig. 5. The *binary–days* method of LFI classification (orange line) peaks at over $\sim 400 \times 10^3\,\mathrm{km}^2$, which is $\sim$65% of the observed maximum. Also improved in this experiment is the FIA min/max timing, compared with observations. In contrast to the delayed and somewhat muted

https://doi.org/10.5194/egusphere-2026-1541
Preprint. Discussion started: 6 May 2026

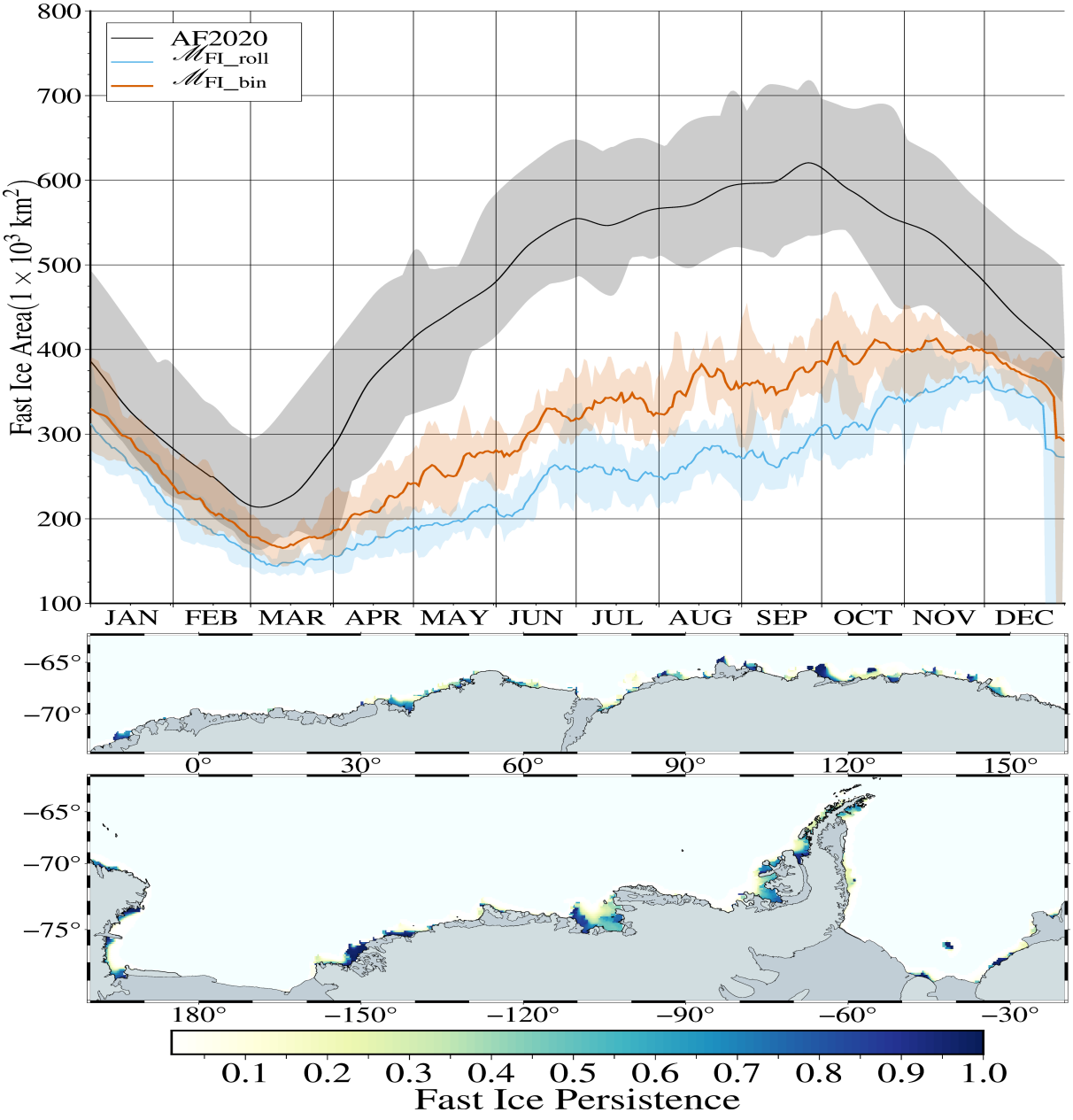

Figure 5. As in Fig. 4, but `gi-mid` adds GIBs ($GIB_\theta = 25\%$) as well as keeping the tensile strength ($k_T = 0.2$).

seasonal cycle of the `notens-nogi` and `gi-nil-def` runs, the inclusion of GIBs in `gi-mid` yields a FIA seasonal cycle whose maximum occurs in the late September through mid–October window and produces a more distinct summer minimum, thereby aligning both the phase and amplitude of the seasonal cycle more closely with F2020. The inclusion of GIBs leads to a substantial increase in both the spatial extent and temporal persistence of modelled LFI across nearly all sectors of the

https://doi.org/10.5194/egusphere-2026-1541
Preprint. Discussion started: 6 May 2026

Antarctic coastline. Notably, the FIP map reveals widespread formation of LFI in East Antarctica, including at key locations: Lützow–Holm Bay, Cape Darnley, Shackleton Ice Shelf, Totten Ice Shelf, and Mertz Glacier Tongue—in general, along much of the East Antarctic coast between 20-160 °E, which are regions that showed near–zero FIP in the absence of GIBs (i.e., CICE6–SA experiments `notens-nogi` and `gi-nil-def`, shown in Figures 3 and 4). This expansion suggests that the presence of a thinned GIB prescription provides sufficient mechanical resistance to inhibit drift and enable the consolidation of landfast in otherwise dynamic environments. Many of these locations correspond with known regions of observed LFI and align closely with high–persistence zones in the F2020 climatology (Fraser et al., 2020).

Together, these results demonstrate that GIBs play a central role in enabling Antarctic LFI formation at the continental scale. While tensile strength alone yields improvements in sheltered regions along the western Antarctic Peninsula, widespread LFI formation and realistic seasonal evolution require the addition of GIBs to provide stability in bathymetrically favourable zones.

Finally, we evaluate the incremental impact of further modifying the yield–curve by lowering the eccentricity parameter from $e = 2.0$ to $e = 1.2$ (i.e., a less elongated yield curve), while retaining all other configurations from the preceding `gi-mid` configuration (for consistency with earlier figures). This experiment, referred to as `elps-min`, includes moderate tensile strength ($k_T = 0.2$) and GIBs ($GIB_\theta = 25\%$), with $P^* = 2.75 \times 10^4$ and $C^* = 20$, and mirrors rheological choices tested in Arctic LFI studies—namely using a lower ellipse aspect ratio with non–zero tensile strength—(e.g., Lemieux et al., 2016, 2018; Panteleev et al., 2020), and aligns with recent Antarctic–focused configurations (e.g., Van Achter et al., 2022). The goal is to assess whether a more isotropic internal–ice–stress–tensor (and modest tensile strength) formulation further improves the representation of Antarctic LFI, as suggested by prior Arctic work linking reduced e to more realistic LFI persistence (Lemieux et al., 2016, 2018).

Fig. 6 shows a $1.65\times$ increase to FIA from `gi-mid` and clear enhancement to spatial distribution of FIP. The top panel reveals a strong increase in FIA across both classification methods, with the *binary–days* estimate achieving values similar to the observed maximum of just over $601 \times 10^3\ km^2$. This experiment notably exceeds the peak extent achieved in the previous (`gi-mid`) simulation, with the spatial distribution of FIP indicating increased presence not only in (aforementioned) key zones across East Antarctica, but also along Prince Olav Coast, West Ice Shelf, Sabrina Coast, Oates Coast, Getz Ice Shelf, and Larsen Ice Shelf. Notably, persistence values reach near–continuous (0.8-1.0) coverage in many grid cells, closely matching observational patterns from F2020. Consistent with the Arctic literature, this suggests that a reduced yield–curve eccentricity enhances the ability of the ice pack to resist internal deformation, thereby facilitating stable LFI formation even in regions with moderate mechanical support (Lemieux et al., 2016). Consistent with previous Arctic and Antarctic studies, reducing yield–curve eccentricity (lower e) enhances FIP and improves the spatial distribution of LFI (Lemieux et al., 2016, 2018; Huot et al., 2021; Van Achter et al., 2022). In our Antarctic experiments, the combination of a reduced e with moderate tensile strength and GIB–induced anchoring produces the most realistic LFI seasonal cycle and persistence patterns among the configurations tested, consistent with the improved agreement with sea–ice thickness in Fig. 1b.

https://doi.org/10.5194/egusphere-2026-1541
Preprint. Discussion started: 6 May 2026

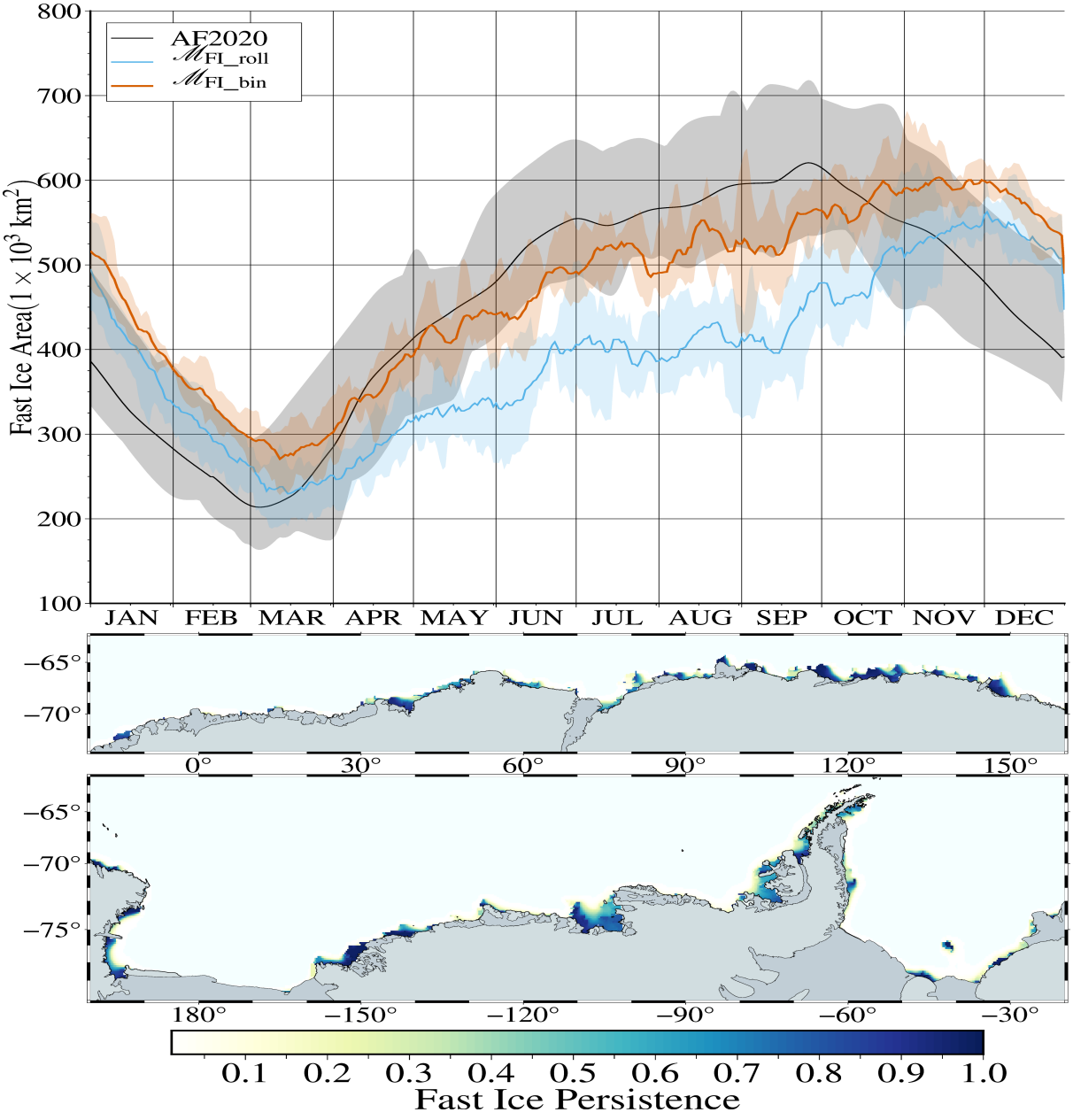

Figure 6. As in Fig. 3, but for the `elps-min` simulation (k_T= 0.2, GIB_θ= 25%, e= 1.2).

3.3 Parameter Sensitivity Sweep

To evaluate how key parameters influence simulated FIA and LFI Thickness (FIT), we vary one parameter at a time—the concentration scaling parameter (C^*), the ice strength parameter (P^*), the tensile strength parameter (k_T), the ellipse aspect

https://doi.org/10.5194/egusphere-2026-1541
Preprint. Discussion started: 6 May 2026

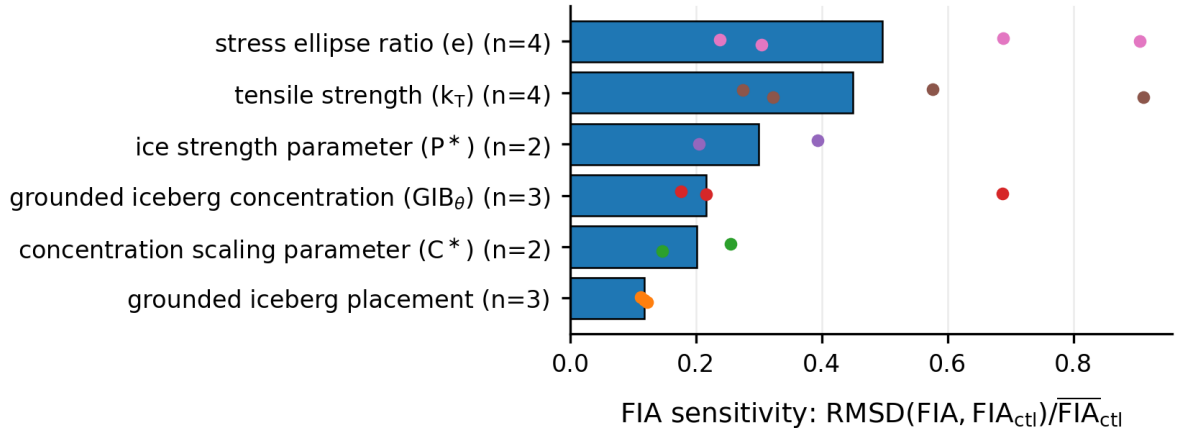

Figure 7. Unitless sensitivity of circumpolar FIA to one–at–a–time parameter perturbations relative to the `gi-mid` control experiment. For each experiment we compute a 1994–1999 fortnightly FIA climatology from the *binary–days* LFI mask ($\mathcal{M}_{\mathrm{FI\_bin}}$) and define sensitivity as $S = \mathrm{RMSD}(\chi_{\mathrm{m}}, \chi_{\mathrm{ctl}})/\overline{\chi_{\mathrm{ctl}}}$, where χ_{m} is the experiment climatology, χ_{ctl} is the control climatology, and $\overline{\chi_{\mathrm{ctl}}}$ is the annual mean of the control climatology. Horizontal bars show the median S across perturbed members within each sweep (the control has $S = 0$ by definition and is omitted from the sweep summary); coloured points show individual members. The GIB fraction sweep (GIB_θ) varies the retained fraction of GIB "island" cells (thinning the GIB landmask), whereas the placement sweep perturbs the spatial arrangement at fixed fraction.

ratio (e), and GIB fraction (GIB_θ)—while holding the others fixed (defaults: $\mathrm{GIB}_\theta = 25\%$, $\mathrm{P}^* = 2.75 \times 10^4$, $\mathrm{C}^* = 20$; Appendix Table E1). For each member we compute daily climatologies of FIA and FIT using the *binary–days* method (W=11, N=9, speed threshold 5×10^{-4} m/s) and then average to 15–day means over 1994–1999 to match the temporal sampling of F2020 (2000–2018). We do not compare FIT directly with ESA–CCI near the Antarctic coast owing to known retrieval uncertainties; instead we use the model spread for context and note published observational ranges (e.g., Fig. 5 of Pirlet et al. 2025). Because FIT is reported as an area–mean over grid cells classified as LFI, changes in FIT can reflect both local thermodynamic differences and shifts in the LFI footprint (e.g., expansion into thinner peripheral ice); thickness differences are therefore interpreted cautiously.

Fig. 7 summarises the sensitivity of the circumpolar FIA climatology to one–at–a–time parameter sweep. Across the explored ranges, the dominant controls on circumpolar FIA are the rheological parameters governing tensile resistance and yield–curve shape: changes in $\mathrm{k_T}$ and e produce the largest departures from the control seasonal cycle. In contrast, the ice–strength scaling parameters P^* and C^* induce smaller changes. The GIB fraction parameter (GIB_θ) shows a moderate sensitivity across the tested non–zero fractions, with the largest step–change occurring between the no–GIB case and the lowest non–zero fraction; by contrast, perturbing GIB placement at fixed fraction produces minimal sensitivity.

Detailed FIA and FIT climatologies for each sweep are provided in Appendix C (Figs. C1–C3).

https://doi.org/10.5194/egusphere-2026-1541
Preprint. Discussion started: 6 May 2026

3.4 Regional Fast Ice Persistence

We compare spatial FIP between the stand–alone CICE6–SA experiment `elps-min` and the satellite–derived F2020 dataset over 2000–2018 using a signed dominance index,

$$D(\mathbf{x}) = \frac{P_{\mathrm{obs}}(\mathbf{x}) - P_{\mathrm{mod}}(\mathbf{x})}{P_{\mathrm{obs}}(\mathbf{x}) + P_{\mathrm{mod}}(\mathbf{x}) + \epsilon}, \tag{2}$$

where P_{obs} and P_{mod} are the per–grid–cell FIP fractions (i.e., the fraction of assessment times classified as LFI) and ϵ is a small constant to avoid division by zero when both are absent. By construction, $D = -1$ indicates LFI occurs only in the model, $D = +1$ indicates LFI occurs only in F2020, and $D \approx 0$ indicates agreement. For compact regional summaries (Table 2), we group D into three bins: *model–dominant* ($D \leq -0.5$), *agreement* ($|D| < 0.5$), and *observation–dominant* ($D \geq 0.5$).

Table 2. Persistence–weighted partitioning of regional FIP differences using the dominance index D (Eq. 2), comparing `elps-min` with F2020 over 2000–2018. Rows are normalised to 100 %. Columns indicate the fraction of regional persistence falling into *agreement* ($|D| < 0.5$), *model–dominant* ($D \leq -0.5$), or *observation-dominant* ($D \geq 0.5$) classes. GIB landmask cells are treated as $P_{\mathrm{mod}} = 100\,\%$ in `elps-min`.

Region	Agreement (%)	Model–dominant (%)	Observation–dominant (%)
Dronning Maud Land sector (DML)	24.7	23.1	52.3
Western Indian Ocean sector (WIO)	45.6	11.0	43.4
Eastern Indian Ocean sector (EIO)	39.8	16.5	43.7
Australian sector (AUS)	51.0	21.0	28.0
Victoria Land sector (VOL)	40.5	23.8	35.8
Amundsen Sea sector (AS)	43.2	20.3	36.5
Bellingshausen Sea sector (BS)	27.6	56.3	16.1
Weddell Sea sector (WS)	34.2	41.2	24.5
Pan–Antarctic	40.5	27.5	32.0

Across Antarctica, 40.5 % of persistence–weighted cells fall into the *agreement* class, 27.5 % are *model–dominant*, and 32.0 % are *observation–dominant* (Table 2). The sector maps (Figs. 8–9) show that these differences organise into coherent coastal belts rather than isolated grid cells. Agreement is highest in the AUS sector (51 %), which is also the sector with the largest observed FIP; strong performance here is therefore particularly encouraging. Agreement is also relatively high in WIO, AS, VOL, and EIO (40-46 %), where $D \approx 0$ commonly occurs along major ice–shelf fronts and prominent coastal promontories that provide anchoring.

Observation–dominant belts ($D > 0.5$) exceed 40 % in DML, WIO, and EIO. These belts preferentially trace geometrically complex coastlines—small capes, fjord–like embayments, and ice–tongue margins—suggesting that some stabilising features and/or local coastal forcing represented in F2020 are under–resolved in the model. In contrast, model–dominant clusters ($D < -0.5$) are strongest in BS and WS, where the model produces extensive LFI within deep embayments and sheltered

https://doi.org/10.5194/egusphere-2026-1541
Preprint. Discussion started: 6 May 2026

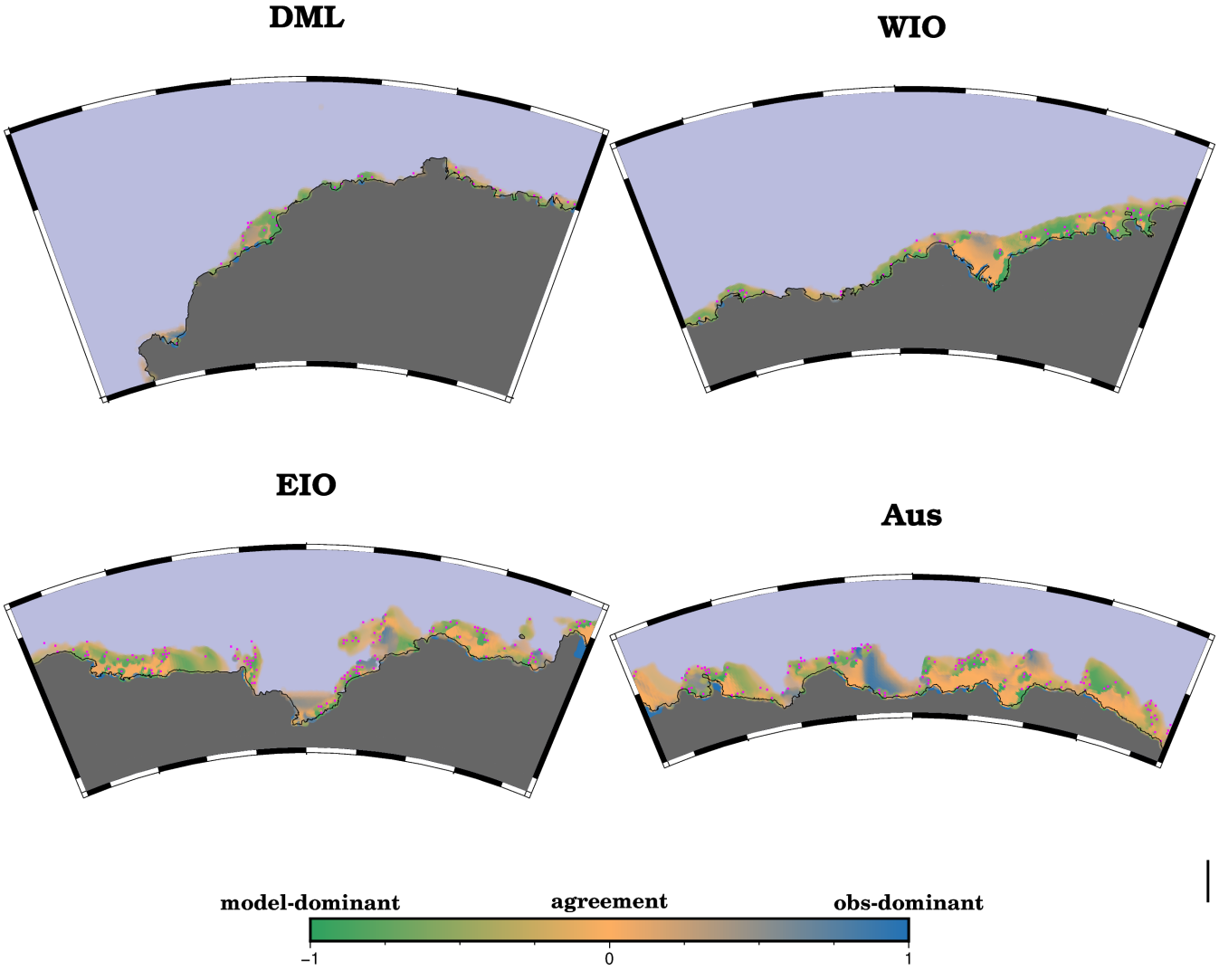

Figure 8. Regional FIP dominance index D (2000–2018) comparing `elps-min` with F2020 for four sectors: DML, WIO, EIO, and AUS. Colours show $D \in [-1, 1]$ (colour bar): $D = -1$ indicates persistence occurs only in the model, $D = 0$ indicates comparable persistence, and $D = +1$ indicates persistence occurs only in F2020. Point opacity is weighted by observed persistence P_{obs}, emphasising locations of persistent–observed LFI. Red squares denote GIB landmask cells in the model.

https://doi.org/10.5194/egusphere-2026-1541
Preprint. Discussion started: 6 May 2026

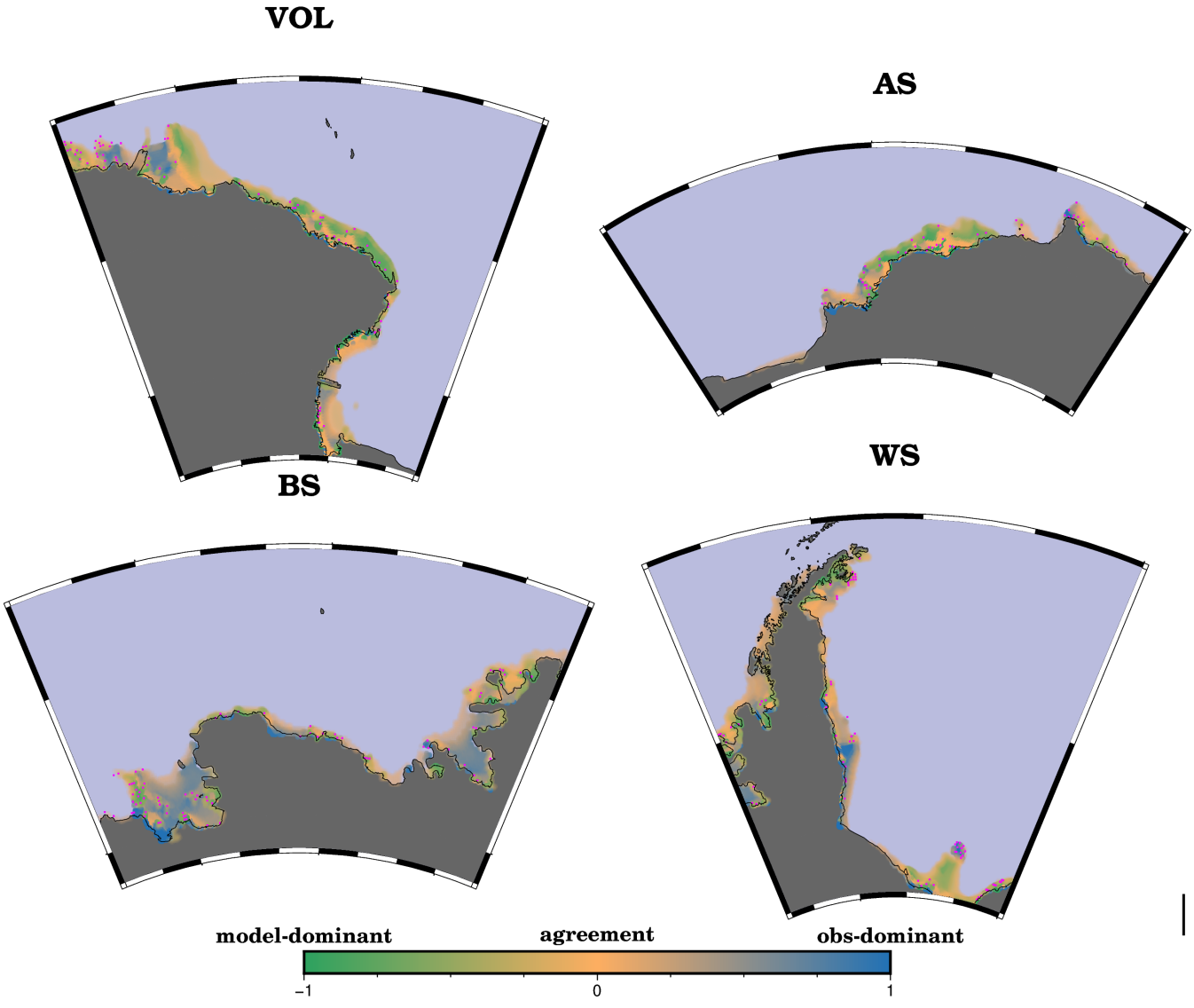

Figure 9. As in Fig. 8, for the remaining four sectors: VOL, AS, BS, and WS. Colours show $D \in [-1, 1]$; opacity is weighted by P_{obs}; red squares mark model GIB landmask cells.

https://doi.org/10.5194/egusphere-2026-1541
Preprint. Discussion started: 6 May 2026

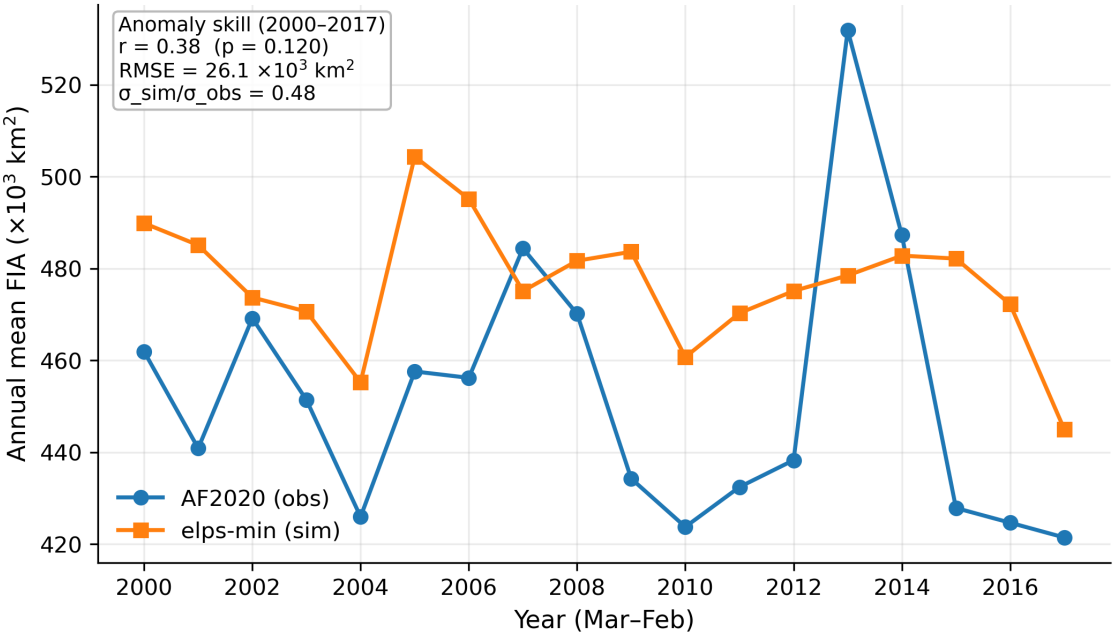

Figure 10. Annual–mean circum–Antarctic LFI Area from F2020 and `elps-min` over the overlap period, computed over March–February "Antarctic years" to avoid partial–year artefacts (2000–2017; $N = 18$). The annotation reports skill for annual anomalies (series mean over the overlap removed): anomaly correlation (r; p–value), anomaly RMSE, and the ratio of simulated to observed anomaly standard deviation.

margins. These patterns may reflect a combination of bathymetric sheltering, weak near–coastal currents, and/or pack–ice conditions that favour multi–year LFI configurations in the model; targeted regional diagnostics (e.g., local bathymetry, coastal winds, and current climatologies) are a natural next step for attributing these clusters.

3.5 Inter–Annual Variability of Circum–Antarctic Fast Ice Area

We assess whether `elps-min` reproduces year–to–year fluctuations in annual–mean circum–Antarctic FIA over the F2020 overlap period (2000–2017; March–February years), and determine that inter–annual variability is captured only weakly. Using annual anomalies (mean removed over 2000–2017), the anomaly correlation between simulated and observed circum–Antarctic FIA is $r = 0.38$ ($p = 0.12$), indicating that the correspondence between year–to–year fluctuations is not statistically significant. The simulated variability is also under–dispersive relative to observations, with $\sigma_{\mathrm{sim}} \approx 14 \times 10^3\,\mathrm{km}^2$ compared with $\sigma_{\mathrm{obs}} \approx 29 \times 10^3\,\mathrm{km}^2$ ($\sigma_{\mathrm{sim}}/\sigma_{\mathrm{obs}} \approx 0.48$).

Additional diagnostics provide a consistent picture. Correlations of annual maximum and minimum FIA are similarly weak ($r_{\max} \approx 0.33$, $r_{\min} \approx 0.34$), suggesting that the model does not reproduce the timing or magnitude of extreme LFI years particularly well. Nevertheless, both the observed and simulated time series exhibit small negative trends over the analysis

https://doi.org/10.5194/egusphere-2026-1541
Preprint. Discussion started: 6 May 2026

period (approximately $-0.6\times10^3\,\mathrm{km^2\,yr^{-1}}$ in the observations and $-0.9\times10^3\,\mathrm{km^2\,yr^{-1}}$ in the simulation), and the simulation remains stable with no systematic drift over the full overlap period (Fig. 10).

Taken together, these results indicate that while the tuned configuration reproduces the mean seasonal behaviour of Antarctic LFI, it underestimates the magnitude of year–to–year variability. This likely reflects missing processes that influence inter–annual LFI stability, such as feedbacks arising from coupling with an ocean model.

3.6 Simulated Fast Ice Dependence on Grounded Iceberg Distribution

To quantify the dependence of simulated Antarctic LFI on GIB anchoring, we introduce a diagnostic metric that measures the fraction of simulated FIA that is no longer present when GIBs are removed from the model configuration. Let $\mathrm{FIA_{GI}}$ denote the FIA simulated in the reference configuration (`elps-min`), and $\mathrm{FIA_{noGI}}$ the FIA simulated in an otherwise identical configuration without GIBs (`gi-nil-def`) present in the model. The GIB dependence fraction is then defined as $D_{\mathrm{GIB}} = \overline{\mathrm{FIA}}_{\mathrm{noGI}}/\overline{\mathrm{FIA}}_{\mathrm{GI}}$, where the over–bar denotes the temporal mean over the analysis period.

Using two of the 1994–1999 simulations analysed in this study (`elps-min` & `gi-nil-def`), the mean circum–Antarctic $\overline{\mathrm{FIA}}_{\mathrm{GI}} \approx 468.7\times10^3\,\mathrm{km^2}$ for the GIB configuration and $\overline{\mathrm{FIA}}_{\mathrm{noGI}} \approx 80.4\times10^3\,\mathrm{km^2}$ without GIBs, hence $D_{\mathrm{GIB}} \approx 0.83$, which indicates $\sim 83\%$ of simulated circum–Antarctic LFI depends on GIB anchoring. The GIB–dependent fraction varies seasonally between approximately 76% and 89% when computing the monthly mean FIA, and results in a climatological mean of $\sim 82\%$, which is very nearly equivalent to the long-term mean.

4 Discussion

The regional FIP–difference maps (Figs. 8–9; Table 2) reveal three coastal regimes: (i) areas where `elps-min` and F2020 agree on fast ice persistence, (ii) belts where observations show greater persistence, and (iii) clusters where the model produces more fast ice than the observations suggest. When considered together with the preceding baseline configuration experiments (Section 3.2) and the parameter sensitivity experiments (Section 3.3), these are consistent with a simple narrative: GIBs are required for producing realistically–modelled Antarctic LFI, and a moderate setting of tensile strength parameter parameterisation and that, once GIBs are present, a moderate value of tensile strength parameter together with a reduced value of the ellipse aspect ratio together regulate the spatial extent and persistence of simulated Antarctic LFI.

The baseline experiment without GIBs and without tensile strength parameter produces almost no circum–Antarctic LFI, with small pockets confined to fjords of the western Antarctic Peninsula. Introducing moderate tensile strength parameter alone only marginally increases circum–Antarctic FIA. The step change occurs when GIBs are added: FIA rises markedly and the seasonal cycle shifts toward the observed winter peak and summer retreat. Reducing the ellipse aspect ratio from 2.0 to 1.2 further improves phase and amplitude of the seasonal cycle and increases spatial continuity of FIP. Quantifying the contrast between simulations with and without GIBs confirms their dominant role as mechanical anchors for Antarctic LFI. Over 1994–1999, mean circum–Antarctic FIA increases from $\approx 80.4\times10^3\,\mathrm{km^2}$ in the no–grounded–iceberg configuration to $\approx 468.7\times10^3\,\mathrm{km^2}$ when GIBs are included. Taken together, these results indicate that although approximately $81-83\%$

https://doi.org/10.5194/egusphere-2026-1541
Preprint. Discussion started: 6 May 2026

of simulated Antarctic LFI depends on GIB, only about half of the simulated LFI lies within the immediate vicinity of mapped GIB anchor points. This difference implies that GIBs exert a stabilising mechanical influence that extends beyond their immediate adjacent grid–cell footprint, enabling the formation and persistence of broader coastal fast–ice systems.

The parameter sensitivity experiments presented in Section 3.3 formalise this picture. Increasing the tensile strength paramter (tensile strength parameter) increases FIA monotonically across the tested parameter range and mainly affects retention through late winter–spring; lowering ellipse aspect ratio promotes coherent persistence with limited effect on thickness; increasing the GIB concentration boosts area across the year. In contrast, C^* and P^* primarily modulate the amplitude of the seasonal FIA cycle within a configuration, without transforming timing or the presence/absence of LFI at the continental scale. These results indicate that GIB, k_T, and e are the principal levers for achieving realistic Antarctic LFI, with GIB acting as the enabling constraint and the two rheological parameters tuning the achievable persistence within that constraint.

Interpreting the spatial departures in the FIP–difference maps in the context of known Antarctic coastal geometries and GIB distributions helps to locate where missing processes are most likely to matter. Where GIB form chains or dense fields, agreement fractions are largest, consistent with prior mapping and synthesis (e.g., Fraser et al., 2020, 2021). Departures associated with time–varying coastal geometry are also apparent. Around the Mertz Glacier region, the February 2010 calving of the Mertz Glacier Tongue and the contemporaneous ungrounding of B9B altered the coastal configuration and nearby fast–ice distribution; observational studies document these changes to coastal sea–ice regimes (Tamura et al., 2012; Massom et al., 2015; Leane and Maddison, 2018). In the southern Weddell Sea, gradual northward migration of A–23A has been linked with the progressive loss of the Weddell fast–ice bridge (Li et al., 2020b); in our static mask A–23A is included but mapped in 2021 after it had already drifted some way to the north, which increases the distance required for fast–ice bridging relative to earlier years. Taken together, these examples suggest that allowing major calving events and large tabular GIBs to update coastal geometry in time is likely to reduce some of the LFI persistent mismatches, while a static treatment remains adequate for smaller GIB whose distribution is comparatively stable. Model–dominant clusters are most prominent in the Bellingshausen Sea sector. A plausible interpretation is that, without an explicit wave–ice breakup pathway, LFI persists in the model in regions that experience long–period swell penetration. The role of swell in flexural failure of Antarctic landfast is documented (Massom et al., 2018; Ochwat et al., 2024) and has roots in earlier accounts of wave–related LFI breakup (Crocker and Wadhams, 1989), with recent assessments also linking swell to large–scale responses along ice–shelf margins (e.g., Liang et al., 2024; Teder et al., 2025; Fraser et al., 2025). We did not simulate waves here; the spatial correspondence between model–dominant regions and areas exposed to swell is therefore presented as hypothesis rather than demonstrated causation. Observation–dominant areas are most extensive along several East Antarctic coasts. A likely explanation is that some GIB that act as LFI anchors remain unresolved in the present model configuration. Recent high–resolution compilations of GIB distributions suggest that additional pinning points may exist along these coastlines, and incorporating these datasets may reduce some of the remaining spatial discrepancies.

Consistent with Fig. 10, `elps-min` captures the mean state of circum–Antarctic FIA reasonably well but reproduces inter–annual variability only weakly. Over the F2020 overlap period (2000–2017), the simulation exhibits a modest positive bias. These results suggest that while the tuned configuration produces a realistic seasonal climatology, additional ingredients

https://doi.org/10.5194/egusphere-2026-1541
Preprint. Discussion started: 6 May 2026

(e.g., time–varying mechanical anchoring, improved coastal forcing, or coupled ocean feedbacks) may be required to reproduce the observed magnitude of inter–annual Antarctic LFI variability.

Introducing GIB into the model as isolated grid cell islands is not the only way to simulate their presence. Other ways of parameterising them can increase resistance to drift along coastlines and promote spontaneous fastening of the pack. One such mechanism is enhanced lateral drag arising from sub-grid scale coastal roughness. A parameterisation representing this effect has recently been implemented in the MITgcm sea ice model (Liu et al., 2022), where increased resistance along complex coastlines slows pack ice motion and facilitates the formation of LFI. We suggest that this approach could be used together with sub–grid–scale GIB maps, to simulate drag associated with observed GIB distributions. In this sense, lateral drag could complement explicit GIB constraints by representing the aggregate anchoring effect of unresolved coastal features and smaller GIB without physically imposing unreaslitic boundary conditions within the model grid.

5 Conclusions

This study identifies the key physical ingredients required for a sea–ice model to reproduce realistic large–scale Antarctic landfast sea ice. A series of experiments demonstrates that the representation of grounded icebergs is the essential modification needed to allow extensive Antarctic fast ice to form. In the absence of grounded icebergs, simulated circum–Antarctic fast–ice area remains extremely small, averaging only $\sim 13\%$, even when rheological parameters are modified to increase tensile strength and reduce the aspect ratio of the yield–curve ellipse. Including grounded icebergs increases the mean simulated fast–ice area to $\sim 67\%$, and, when combined with enhanced tensile strength and a reduced yield–curve ellipse aspect ratio, produces a near–equivalent circum–Antarctic fast–ice area. However, inter–annual variability is not well reproduced, likely because grounded icebergs are implemented in a static manner and the simulations do not include feedbacks from a coupled ocean. Considering the effect of grounded icebergs alone, we find that $\sim 83\%$ of simulated fast–ice area depends on their presence as mechanical anchoring points.

Once grounded icebergs are present, rheological parameters determine how fast ice evolves and persists. In particular, the tensile strength parameter (k_{tens}) allows the ice cover to remain attached, while reducing the ellipse aspect ratio (e) promotes spatially coherent persistence without substantially altering simulated ice thickness. Parameter sensitivity experiments confirm that these two parameters primarily control the seasonal amplitude and phase of circum–Antarctic fast–ice area, whereas the traditional ice–strength parameters C^* and P^* exert only secondary influence on large–scale fast–ice behaviour. Lowering P^* additionally produces unrealistic reductions in fast–ice thickness. The configuration that combines moderate tensile strength, grounded iceberg representation, and a reduced ellipse aspect ratio ($\mathrm{k_T} = 0.2$, $\mathrm{GIB}_\theta = 25\%$), and $\mathrm{e} = 1.2$), with ice strength and ice concentration scaling parameters ($\mathrm{P}^* = 2.75 \times 10^4$ and $\mathrm{C}^* = 20$) produces the most realistic circum–Antarctic fast–ice area and persistence among the simulations tested. Notably, these parameter values are broadly consistent with those commonly used in Arctic sea–ice applications, lending confidence that the rheological behaviour required to simulate fast ice globally is physically consistent, rather than strongly region–specific.

https://doi.org/10.5194/egusphere-2026-1541
Preprint. Discussion started: 6 May 2026

Evaluation against the observational fast–ice record of Fraser et al. (2020) shows that the tuned configuration reproduces the large–scale seasonal cycle of Antarctic fast ice and captures part of the observed interannual variability. Over the 2000–2017 overlap period, the model exhibits a small, insignificant positive bias in mean fast–ice area, reproducing year–to–year variability partially (anomaly correlation $r = 0.38$, $p = 0.120$, $\sigma_{\mathrm{sim}}/\sigma_{\mathrm{obs}} \approx 0.48$). In particular, the model does not reproduce the large observed positive anomalies during 2013–2014 and underestimates the magnitude of the subsequent decline toward 2015–2017. These results indicate that while the present configuration captures the mean seasonal behaviour of Antarctic fast ice, additional processes are likely required to reproduce the full magnitude of interannual variability.

Spatial comparisons of fast–ice persistence between simulations and observations further highlight where such processes may be important. Agreement is highest along coastlines where grounded icebergs form dense chains or clusters, reinforcing their role as primary anchoring points for fast ice. Persistent mismatches occur where coastal geometry changed during the study period—for example following the 2010 calving of the Mertz Glacier Tongue and the ungrounding of iceberg B9B, or during the northward migration of iceberg A–23A in the southern Weddell Sea. These patterns suggest that allowing major calving events and large tabular icebergs to modify the coastal geometry through time may reduce some of the remaining discrepancies. Additional mismatches occur along swell–exposed margins such as the Bellingshausen Sea, where wave–induced breakup of fast ice has been observed but is not represented in the present model configuration.

Together, these results outline a clear pathway for improving Antarctic fast–ice simulation in sea–ice models. Future development should focus on representing time–varying grounded–iceberg geometry associated with major calving events and large tabular icebergs, evaluating parameterisations of wave–induced fast–ice breakup in swell–exposed regions, and exploring lateral drag formulations that represent resistance from unresolved grounded iceberg fields without artificially blocking ocean circulation. Coupling the sea–ice model to a dynamic ocean is also likely to improve the representation of coastal currents, thermodynamic feedbacks, and ice–ocean interactions that influence fast–ice stability. Implemented together, these developments offer a realistic path toward more faithful simulation of Antarctic landfast ice in both present–day and future climate experiments.

https://doi.org/10.5194/egusphere-2026-1541
Preprint. Discussion started: 6 May 2026

Appendix A: Grounded Iceberg Dataset Creation

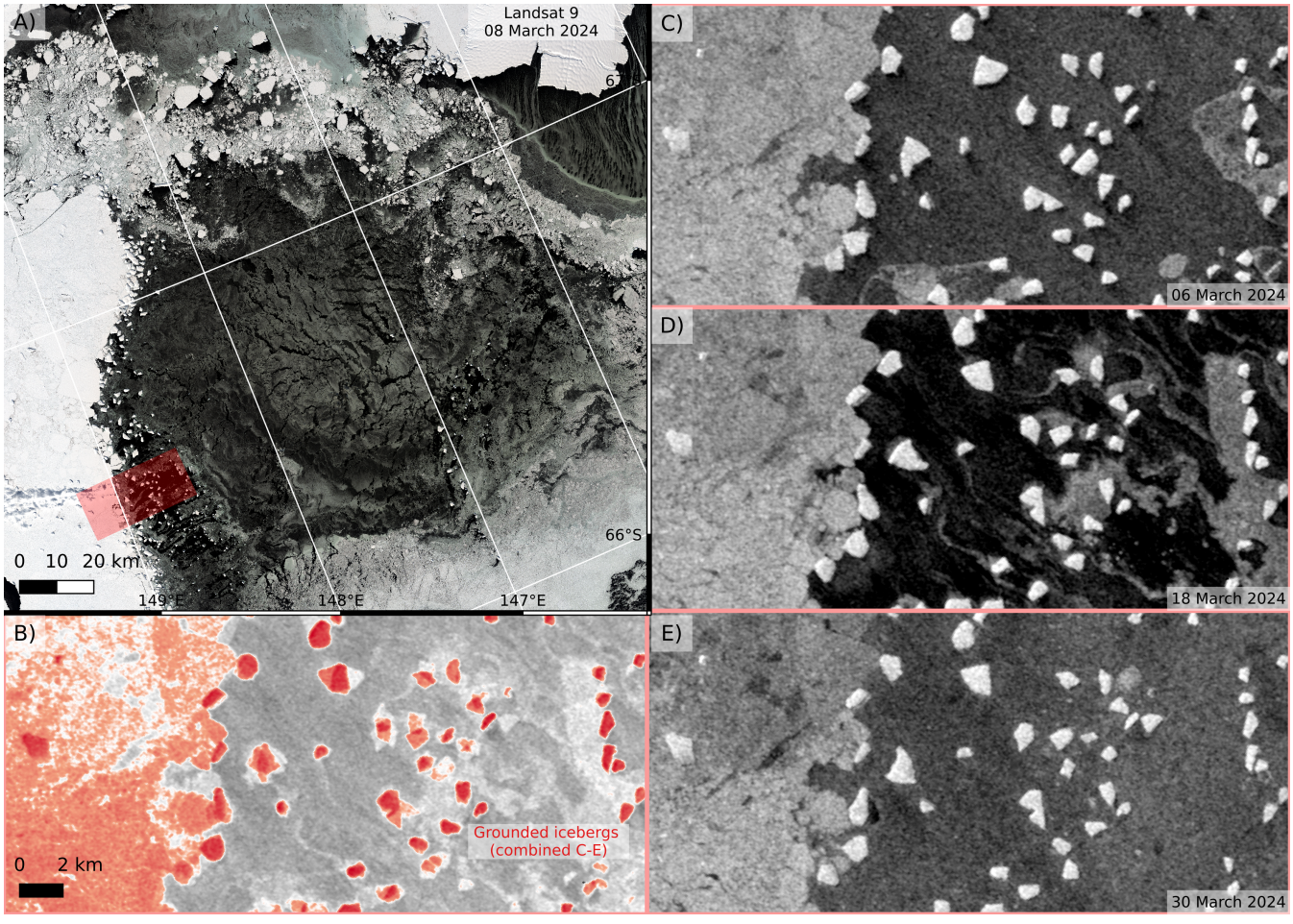

Figure A1. Example of GIBs at Ninnis Bank ($66-68^{\circ}$S, $146-150^{\circ}$E) during March 2024 using satellite imagery. A) A Landsat–9 true–colour composite image from 8 March, 2024 showing the coastal environment, with the red inset indicating the area examined in subsequent panels. B) Colour–enhanced composite map showing GIB locations (dark red) derived from the SAR backscatter analysis. C–E) Corresponding Sentinel–1A SAR Extra Wide Swath (EW) (polarisation HH) imagery acquired on 6, 18, and 30 March, highlighting areas of high backscatter from icebergs.

https://doi.org/10.5194/egusphere-2026-1541
Preprint. Discussion started: 6 May 2026

GIBs were manually identified using Sentinel–1A SAR EW (polarisation HH) data acquired during the austral summer LFI minimum in March 2024 (Fraser et al., 2021). This period was selected to minimise the number of icebergs which were held stationary within LFI, since this is the climatological time of minimum LFI extent. As such, stationary icebergs that remained outside the surrounding LFI cover were interpreted as the most likely grounded candidates at this time of year. The year 2024 was selected because, at the time, this was the lowest extent of LFI in the observational record (Abram et al., 2025).

Fig. A1 panel A) shows a Landsat–9 true–colour composite (8 March 2024), used for context. Panels C–E contain radiometrically terrain corrected Sentinel–1A EW SAR scenes (acquired on 6, 18, and 30 March, 2024). This time period occurs after most melt has refrozen, giving a large backscatter contrast between sea ice/ocean (relatively low backscatter) and icebergs (high backscatter).

Analysis–ready Sentinel–1 EW SAR data were provided by Geoscience Australia under the Digital Earth Antarctica Program. Sentinel–1 EW Ground Range Detected (GRD) data were processed to a normalised, radiometrically terrain–corrected gamma–nought backscatter product using the pyroSAR (Truckenbrodt et al., 2019) and GAMMA (GAMMA Remote Sensing AG, 2024) software packages. Processing used the Copernicus $30\,\mathrm{m}$ Digital Elevation Model (DEM), with ellipsoidal heights applied for offshore data. The data were produced in decibel scaling at $40\,\mathrm{m}$ spatial resolution and reprojected to polar stereographic coordinates for analysis. Default range and azimuth multi–looking parameters defined by pyroSAR were used. GRD border noise was removed from the input data using the pyroSAR method, and the bicubic spline back–geocoding method was applied.

Manual detection of GIB was based on the requirement that a high–backscatter feature exhibit spatial persistence across three SAR acquisitions in March 2024. To mitigate high labour costs associated with manual selection of thousands of GIBs, the SAR imagery was processed to enhance temporally–persistent high–backscatter features by stacking time–separated images and applying intensity normalisation and colour stretching techniques (see Fig. A1b). The resulting dataset, representing the first circum–Antarctic dataset of grounded iceberg locations, is presented as part of this manuscript, and contains the manually-extracted locations of over 6,500 GIBs around Antarctica.

The conversion of the GIB point dataset into a model–ready mask was carried out using the AFIM (Atwater, 2026a) analysis framework archived with this manuscript. To translate this GIB database into a form suitable for CICE6–SA use, two steps were carried out:

1. each GIB centre position was assigned to the nearest model grid cell using a nearest–neighbour search, and GIB counts were then accumulated within each model grid cell; and

2. a probabilistic thinning algorithm was applied to the set of model grid cells containing one or more GIBs.

The aim of this approach was to preserve the large–scale spatial distribution and regional density of GIB while using an automated method to reduce the total number of cells that would be converted to land “islands” in the model. This was essential to avoid unrealistic obstructions to ocean circulation and excessive LFI formation due to over–anchoring. This kind of “thinning” has also been applied by (Van Achter et al., 2022), but was performed manually in that work.

https://doi.org/10.5194/egusphere-2026-1541
Preprint. Discussion started: 6 May 2026

The thinning probability p was defined using a scaled, non–linear function of GIB count per grid cell:

$$p = p_{\min} + \left(\frac{c - c_{\min}}{c_{\max} - c_{\min}} \right)^{\gamma} (p_{\max} - p_{\min}), \tag{A1}$$

where c is the local iceberg count, $p_{\min}$ and $p_{\max}$ are the minimum and maximum retention probabilities, and γ is a steepness control exponent (set to 2.0 to favour a quadratic relationship and keep the probabilities easily comparable to a concentration range between 0 and 1). This function ensures that regions with few icebergs have a low retention probability, while high–density areas are preferentially preserved. This yielded a geographically balanced field of retained GIB cells ("islands"), while preserving the large-scale regional density structure of the original dataset across repeated applications of the same settings. To ensure representation of solitary GIBs, which may still provide important anchoring points for LFI, any cell with no neighbouring GIB was retained regardless of its thinning probability. Let $M(i,j)$ be the binary GIB mask, where $M = 1$ denotes a GIB and $M = 0$ indicates its absence. A cell at position (i,j) is defined as *isolated* if all of its eight immediately adjacent neighbours contain no GIB:

$$M(i+\delta_i, j+\delta_j) = 0 \quad \text{for all} \quad (\delta_i, \delta_j) \in \{(-1,-1), (-1,0), (-1,1), (0,-1), (0,1), (1,-1), (1,0), (1,1)\}. \tag{A2}$$

If this condition holds, the cell at (i,j) is retained in the final mask regardless of its assigned thinning probability. This conditional rule ensures that even isolated GIB cells can serve as anchoring points for LFI in otherwise sparse regions, consistent with observations of individual GIB stabilising local LFI formation. The final GIB_θ mask was used to update the CICE6–SA landmask file, reclassifying retained iceberg cells as land.

Appendix B: Justification of Model Fast Ice Classification Method

B1 Re–gridding Ice Velocities

To accurately represent sea ice motion near coastlines, we must address the implications of the *no–slip boundary condition* implemented in the CICE6–SA configuration. In the Arakawa B–grid, sea ice velocity components $(u_{\text{ice}}, v_{\text{ice}})$ are defined at cell corners, while scalar variables such as concentration (A_{ice}) are defined at cell centres (the T–grid) (Murray, 1996; Hunke et al., 2022). This staggering can introduce artefacts when comparing fields directly: land–adjacent B–grid velocity points are artificially set to zero by the no–slip condition, producing "dead zones" in computed ice–speed fields immediately west, southwest, and south of the coastline. For LFI classification, we therefore require a T–grid representation of ice speed that is co–located with concentration and does not inherit corner artefacts from the B–grid.

In this study, we compute the native B–grid speed magnitude

$$|\boldsymbol{u}_B| = \sqrt{u_{\text{ice}}^2 + v_{\text{ice}}^2}, \tag{B1}$$

and then construct several T–grid approximations of speed from the underlying velocity components:

https://doi.org/10.5194/egusphere-2026-1541
Preprint. Discussion started: 6 May 2026

- a simple 2×2 box average (`Ta`), obtained by averaging u_{ice} and v_{ice} over the four neighbouring B–grid corners around each T–point;
- a no–slip–aware 2×2 average (`Tb`), which treats land–corner values as zero before averaging, thereby preserving the intended no–slip behaviour while smoothing isolated corner artefacts; and
- a bilinear B→T regridding (`Tx`), performed with precomputed ESMF weights and then combined into a magnitude field.

For a generic B–grid velocity component $\mathrm{q_B} \in \{\mathrm{u_{ice}}, \mathrm{v_{ice}}\}$, the `Ta`–averaged T–grid value at cell centre $(i+\frac{1}{2}, j+\frac{1}{2})$ is

$$\mathrm{q_{T_a}}\left(i+\tfrac{1}{2}, j+\tfrac{1}{2}\right) = \frac{1}{4}\left[\mathrm{q_B}(i,j) + \mathrm{q_B}(i+1,j) + \mathrm{q_B}(i,j+1) + \mathrm{q_B}(i+1,j+1)\right]. \tag{B2}$$

The corresponding `Ta`–speed magnitude is then

$$\left|\mathbf{u}_{\mathrm{T_a}}\right| = \sqrt{\mathrm{u}_{\mathrm{T_a}}^2 + \mathrm{v}_{\mathrm{T_a}}^2}. \tag{B3}$$

For `Tb`, we first enforce the no–slip condition at land corners by defining

$$\mathrm{q_B^{(ns)}}(i,j) = \begin{cases} \mathrm{q_B}(i,j), & \text{if the B–grid corner } (i,j) \text{ is ocean,} \\ 0, & \text{if the B–grid corner } (i,j) \text{ is land,} \end{cases} \tag{B4}$$

where $\mathrm{q_B} \in \{\mathrm{u_{ice}}, \mathrm{v_{ice}}\}$. The `Tb`–averaged T–grid value at the cell centre $(i+\frac{1}{2}, j+\frac{1}{2})$ is then

$$\mathrm{q_{T_b}}\left(i+\tfrac{1}{2}, j+\tfrac{1}{2}\right) = \frac{1}{4}\left[\mathrm{q_B^{(ns)}}(i,j) + \mathrm{q_B^{(ns)}}(i+1,j) + \mathrm{q_B^{(ns)}}(i,j+1) + \mathrm{q_B^{(ns)}}(i+1,j+1)\right]. \tag{B5}$$

In particular, for a T–cell with a coast immediately to the south, the two southern B–grid corners are land and hence contribute zeros to the numerator while the denominator remains 4. The corresponding `Tb`–speed magnitude is

$$\left|\mathbf{u}_{\mathrm{T_b}}\right| = \sqrt{\mathrm{u}_{\mathrm{T_b}}^2 + \mathrm{v}_{\mathrm{T_b}}^2}. \tag{B6}$$

The classification framework is written to allow a composite T–grid speed formed from any subset of {`B`, `Ta`, `Tb`, `Tx`}, but for the experiments analysed in this paper we use the `Tb` field exclusively as the LFI diagnostic. In practice, this amounts to defining LFI where

$$\mathrm{A_{ice}} > \mathrm{A_{thresh}} \quad \text{and} \quad 0 < \left|\mathbf{u}_{\mathrm{Tb}}\right| \leq \mathrm{u_{thresh}}, \tag{B7}$$

with $\mathrm{A_{thresh}}$ and $\mathrm{u_{thresh}}$ given in Section 3.3. The `Tb` construction suppresses unphysical "dead" velocity cells adjacent to land while retaining the physically motivated no–slip condition and ensuring that concentration and speed are evaluated on the same T–grid. This step is specific to the B–grid implementation used here; future simulations employing CICEs emerging C–grid formulation may be able to avoid such an intermediate regridding. These diagnostics and classification workflows were implemented in the AFIM analysis framework archived with this manuscript (Atwater, 2026a).

https://doi.org/10.5194/egusphere-2026-1541
Preprint. Discussion started: 6 May 2026

B2 Rolling Mean and Binary–Day Fast Ice Classification Methods

Within AFIM (Atwater, 2026a), two temporal classification methods are applied to CICE6–SA model output to classify LFI: a *rolling–mean* method and a *binary–days* persistence method. In the *rolling–mean* approach, tracer and velocity fields are smoothed using a centred 15–day window. A cell is classified as LFI if ice concentration exceeds $\alpha = 0.15$ and the smoothed ice speed derived from $\boldsymbol{u}_{Tb}$ is greater than machine–zero but less than or equal to $\beta = 5 \times 10^{-4}\,\mathrm{m/s}$. This yields a mask:

$$\mathcal{M}_{\mathrm{FI\_roll}}(t,i,j) = \begin{cases} 1, & \text{if } A_{\mathrm{ice}}(t,i,j) > \alpha \text{ and } 0 < \|\overline{\boldsymbol{u}_{Tb}}(t,i,j)\| \leq \beta, \\ 0, & \text{otherwise.} \end{cases} \tag{B8}$$

In the *binary–days* method, we evaluate the classification daily (no smoothing), again using the same concentration and speed thresholds:

$$\mathcal{M}_{\mathrm{FI\_day}}(t,i,j) = \begin{cases} 1, & \text{if } A_{\mathrm{ice}}(t,i,j) > \alpha \text{ and } 0 < \|\boldsymbol{u}_{Tb}(t,i,j)\| \leq \beta, \\ 0, & \text{otherwise.} \end{cases} \tag{B9}$$

To capture persistence, we then apply a temporal filter to the daily binary classification:

$$\mathcal{M}_{\mathrm{FI\_bin}}(t) = \begin{cases} 1, & \text{if } \displaystyle\sum_{k=-W/2}^{W/2} \mathcal{M}_{\mathrm{FI\_day}}(t+k) \geq N, \\ 0, & \text{otherwise.} \end{cases} \tag{B10}$$

with nominal values $W = 11$ and $N = 9$ used in the main text, though other parameter values are explored (see below).

B3 Justification for Ice Speed Threshold β

Fig. B1 illustrates the sensitivity of simulated FIA to the choice of ice speed threshold β, using both the *binary–days* and *rolling–mean* classification methods. The *binary–days* method uses $W = 11$, $N = 9$, while the *rolling–mean* method uses a $15\,\mathrm{d}$ rolling average. The results are taken from the `elps-min` simulation, and the annual circum–Antarctic FIA minima/-maxima values are then averaged over 1994–2023 period. At very low thresholds ($\beta \lesssim 10^{-4}\,\mathrm{m/s}$), only the most immobile ice is classified as fastened. This leads to unrealistically small values of FIA, below the observed circum–Antarctic bounds (black dashed lines, of observed climatological circum–Antarctic FIA min/max from F2020). As β increases, progressively more sea ice is classified as LFI, producing higher simulated FIA values. Beyond $\sim 10^{-3}\,\mathrm{m/s}$, the classification begins to encompass large areas of pack ice that are still mobile, resulting in an overestimate of FIA. The behaviour is not entirely smooth: curves flatten or show small discontinuities where regional maxima and minima change between years. This reflects the stepwise nature of LFI classification at the scale of model grid cells, rather than an artefact of the method. Importantly, both classification methods asymptote to stable FIA ranges at higher thresholds.

The vertical gray dashed line marks $\beta = 5 \times 10^{-4}\,\mathrm{m/s}$, a two–week *rolling–mean* criterion commonly adopted in earlier studies (e.g., Lemieux et al., 2016; Huot et al., 2021; Van Achter et al., 2022). At this value, the *rolling–mean* method yields

https://doi.org/10.5194/egusphere-2026-1541
Preprint. Discussion started: 6 May 2026

FIA maxima that lie near the upper bound of observed estimates from Fraser et al. (2021), while maintaining minima that remain well below the observed range, consistent with seasonal LFI retreat. The *binary–days* method produces a slightly higher estimate of FIA maxima at this threshold, but both methods remain within the plausible observational window. Overall, we adopt $\beta = 5 \times 10^{-4}$ m/s as a physically defensible compromise: it excludes mobile pack ice, avoids the unrealistically low coverage from more stringent thresholds, and yields annual FIA maxima and minima consistent with observations.

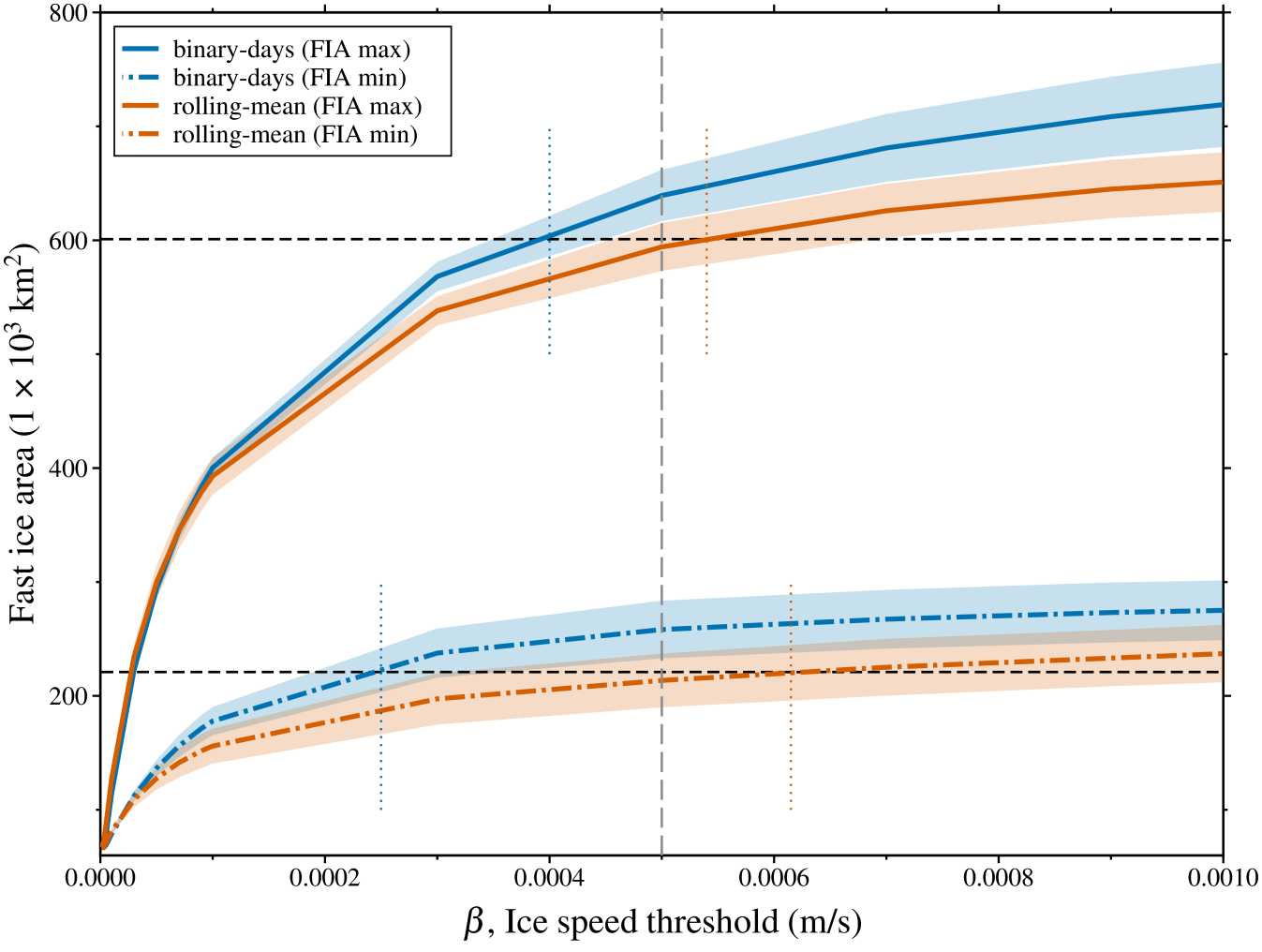

Figure B1. Sensitivity of simulated LFI Area minima and maxima from `elps-min` (1994–2023 average) to the ice speed threshold β. Both *binary–days* (blue and yellow) and *rolling–mean* (green and red) methods are shown. Vertical coloured dashed lines denote where the circum–Antarctic simulated FIA min/max lines intersect with the observed circum–Antarctic FIA min/max from Fraser et al. (2021). The vertical gray dashed line marks $\beta = 5 \times 10^{-4}$ m/s, as used by Lemieux et al. (2016).

https://doi.org/10.5194/egusphere-2026-1541
Preprint. Discussion started: 6 May 2026

B4 Fast Ice Classification Method Comparison

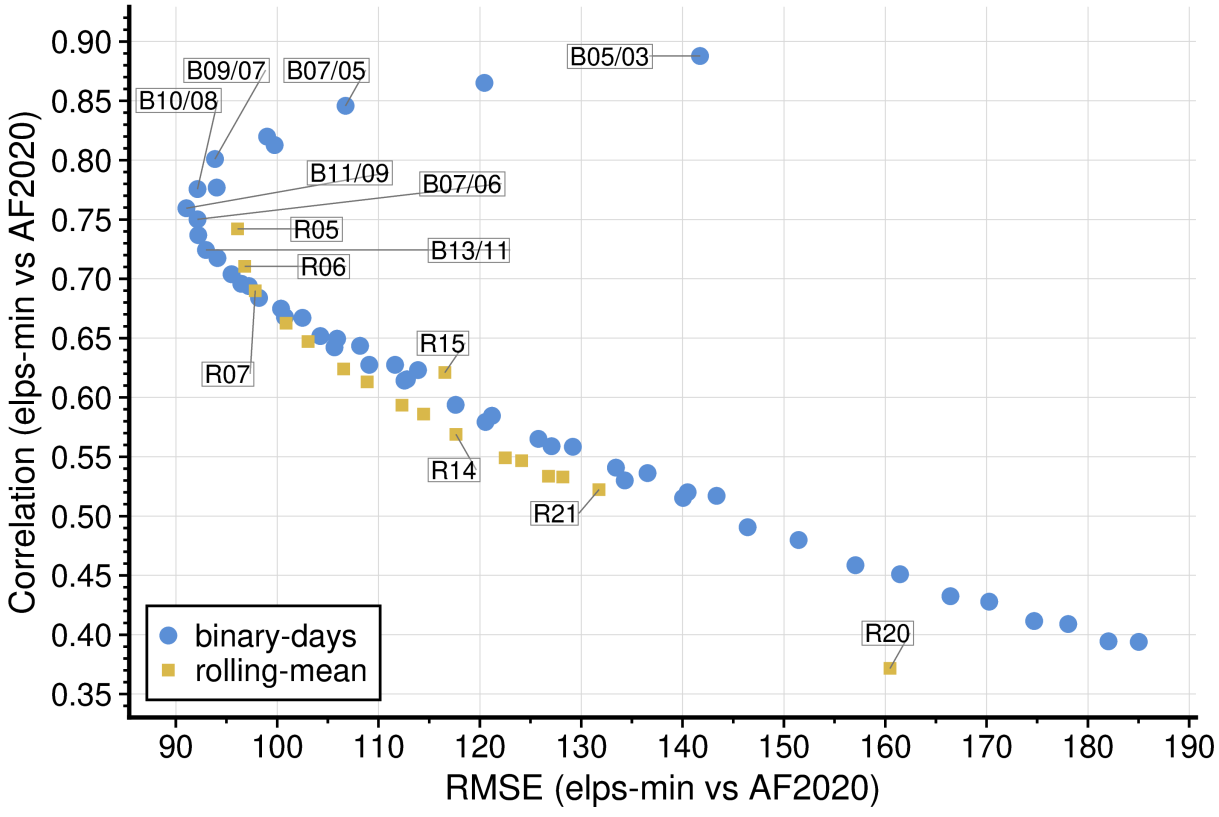

Figure B2. Trade–off between RMSE and correlation for fast–ice classification configurations, evaluated against observed circum–Antarctic FIA from F2020 over 1994–1999. Circles denote *binary–days* methods and squares denote *rolling–mean* methods; marker size is proportional to the absolute FIA bias. For compactness, *binary–days* configurations are labelled as BW/N, meaning N days classified as fast ice within a W–day window, while *rolling–mean* configurations are labelled as Rk for a k–day averaging window. The annotated points identify representative configurations discussed in the text.

Fig. B2 compares the skill of the *binary–days* and *rolling–mean* fast–ice classification methods using annual circum–Antarctic FIA over 1994–1999. A clear trade–off is evident between RMSE and correlation: configurations with the highest correlations tend to occur at larger RMSE, whereas those with the lowest RMSE generally exhibit more moderate correlation. Across most of the skill space, however, the *binary–days* family forms the upper performance envelope, achieving higher correlation than the *rolling–mean* family at comparable RMSE.

The annotated *binary–days* configurations highlight this behaviour. Very permissive persistence criteria, such as B05/03 and B07/05, attain the largest correlations, but only at substantially increased RMSE. At the opposite end of the trade–off, configurations such as B10/08 and B09/07 occupy the lowest–RMSE part of the binary–days family, albeit with weaker correlation.

https://doi.org/10.5194/egusphere-2026-1541
Preprint. Discussion started: 6 May 2026

Intermediate configurations, including B11/09 and B13/11, sit between these extremes and therefore provide a more balanced compromise between amplitude error and temporal agreement.

The *rolling–mean* family follows a similar progression with increasing window length, but is consistently displaced toward lower correlation relative to *binary–days*. Shorter rolling windows, such as R05–R07, provide the strongest *rolling–mean* performance, whereas longer windows (e.g., R14, R15, R20, and R21) move toward progressively weaker correlation and larger RMSE. This indicates that temporal smoothing alone is less effective than an explicit persistence criterion for reproducing observed circum–Antarctic FIA variability.

On this basis, the *binary–days* method is preferred for the analyses presented in this study. In particular, B11/09 (9 days of attachment within an 11–day window) is retained as the adopted configuration because it lies within the cluster of well–performing binary–days solutions while avoiding the larger RMSE associated with the shortest, most permissive persistence windows. Physically, this corresponds to requiring sustained attachment over approximately 1.5 weeks, which is more consistent with the expected persistence of LFI than classifications dominated by short–lived episodes of low ice speed.

Table B1. Skill metrics for selected configurations comparing simulated FIA (CICE6–SA `elps-min`) against observations (1994–1999).

Configuration	Bias	MAE	RMSE	Corr
binary–days W=10, N=8	39.1	72.0	89.3	0.804
binary–days W=11, N=9	28.2	72.3	88.6	0.782
binary–days W=12, N=10	18.6	73.0	88.1	0.769
rolling–mean W=11	−18.4	90.3	104.9	0.642

Appendix C: Sensitivity sweep climatologies

Minor end–of–year features (late December) are sensitive to the 15–day averaging and the persistence—window classification near the seasonal transition; we therefore emphasise the February–November behaviour when interpreting parameter effects.

C1 C^* (concentration scaling)

Fig. C1a–b summarises sensitivity to the concentration scaling parameter C^*. In the Hibler ice—strength formulation, C^* appears in the exponential term $\mathrm{P} \propto \exp[-\mathrm{C}^*(1-A)]$, where A is ice concentration; it therefore controls how rapidly internal strength decays as concentration falls below unity. Smaller C^* values maintain higher strength at intermediate concentrations, while larger C^* values produce a weaker pack for the same mean thickness. As a result, tuning C^* (together with P^*) has been used in Arctic applications to reduce drift and thickness biases and better match observed large–scale sea–ice properties (e.g., Hibler, 1979; Ungermann et al., 2017; Bouchat et al., 2022).

In panel a, all three CICE6–SA members remain well below the observed FIA envelope, indicating that C^* alone cannot remove the low bias in circum–Antarctic FIA. Reducing C^* yields a modest, nearly uniform increase in FIA through the

https://doi.org/10.5194/egusphere-2026-1541
Preprint. Discussion started: 6 May 2026

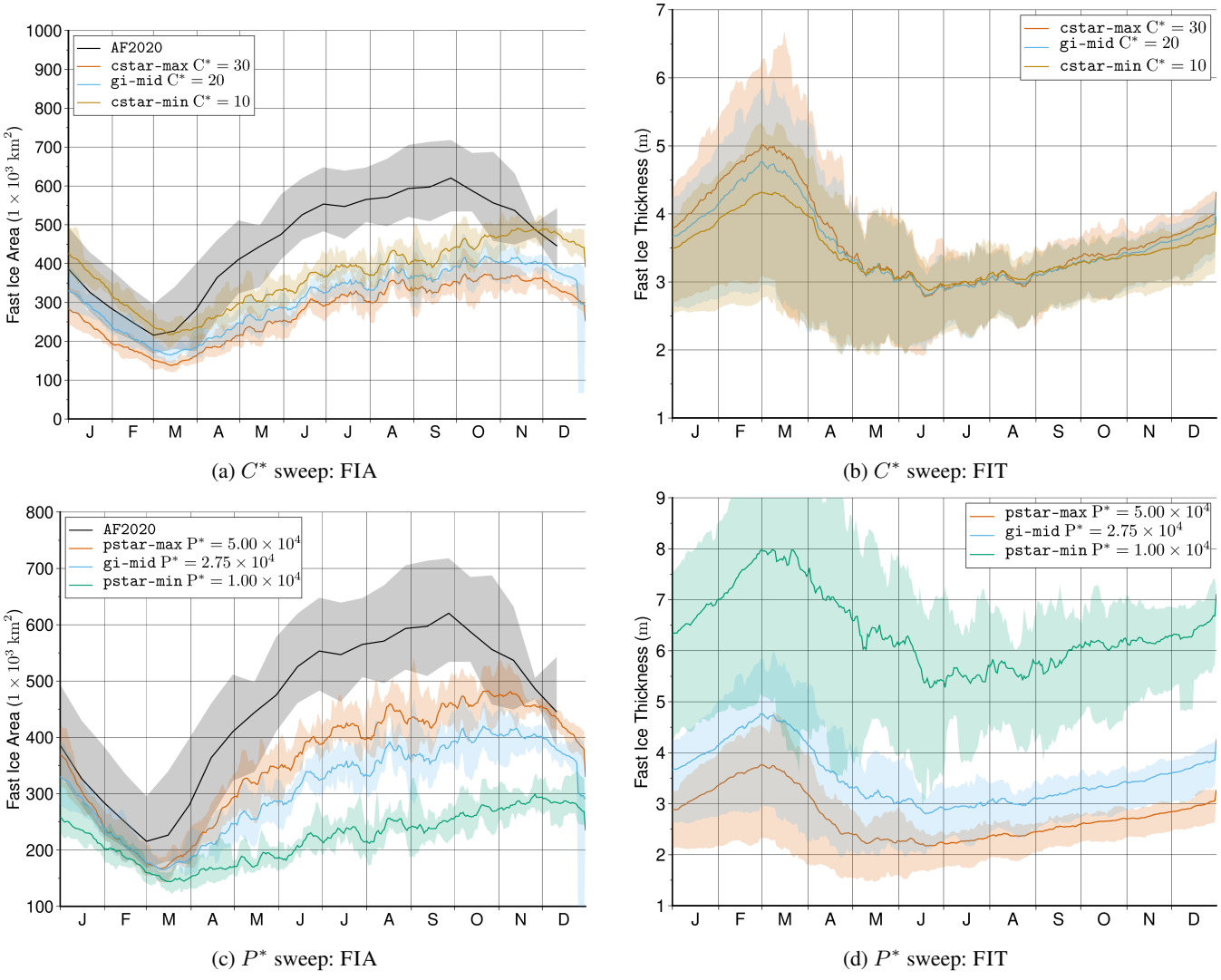

(a) C^* sweep: FIA

(b) C^* sweep: FIT

(c) P^* sweep: FIA

(d) P^* sweep: FIT

Figure C1. One–at–a–time rheology sweeps showing 1994–1999 15–day mean climatologies of circumpolar FIA and area–mean FIT over the diagnosed *binary–days* LFI mask.

year, with slightly earlier winter growth and a marginally larger spring peak; the phase of the seasonal cycle changes little. Panel b shows that area–mean FIT differs slightly across members, consistent with changes in which grid cells satisfy the LFI criterion (e.g., expansion into thinner peripheral zones versus contraction toward thicker core zones), while seasonal timing is essentially unchanged. Model FIT is systematically high (roughly twice the values reported near Syowa Station by Pirlet et al. 2025), plausibly linked to the CICE6–SA configuration (fixed mixed–layer depth and missing coupled ocean feedbacks that would increase basal heat flux and export). Taken together, FIA is only weakly sensitive to C*, and FIT differences across C* are small relative to the overall model spread.

https://doi.org/10.5194/egusphere-2026-1541
Preprint. Discussion started: 6 May 2026

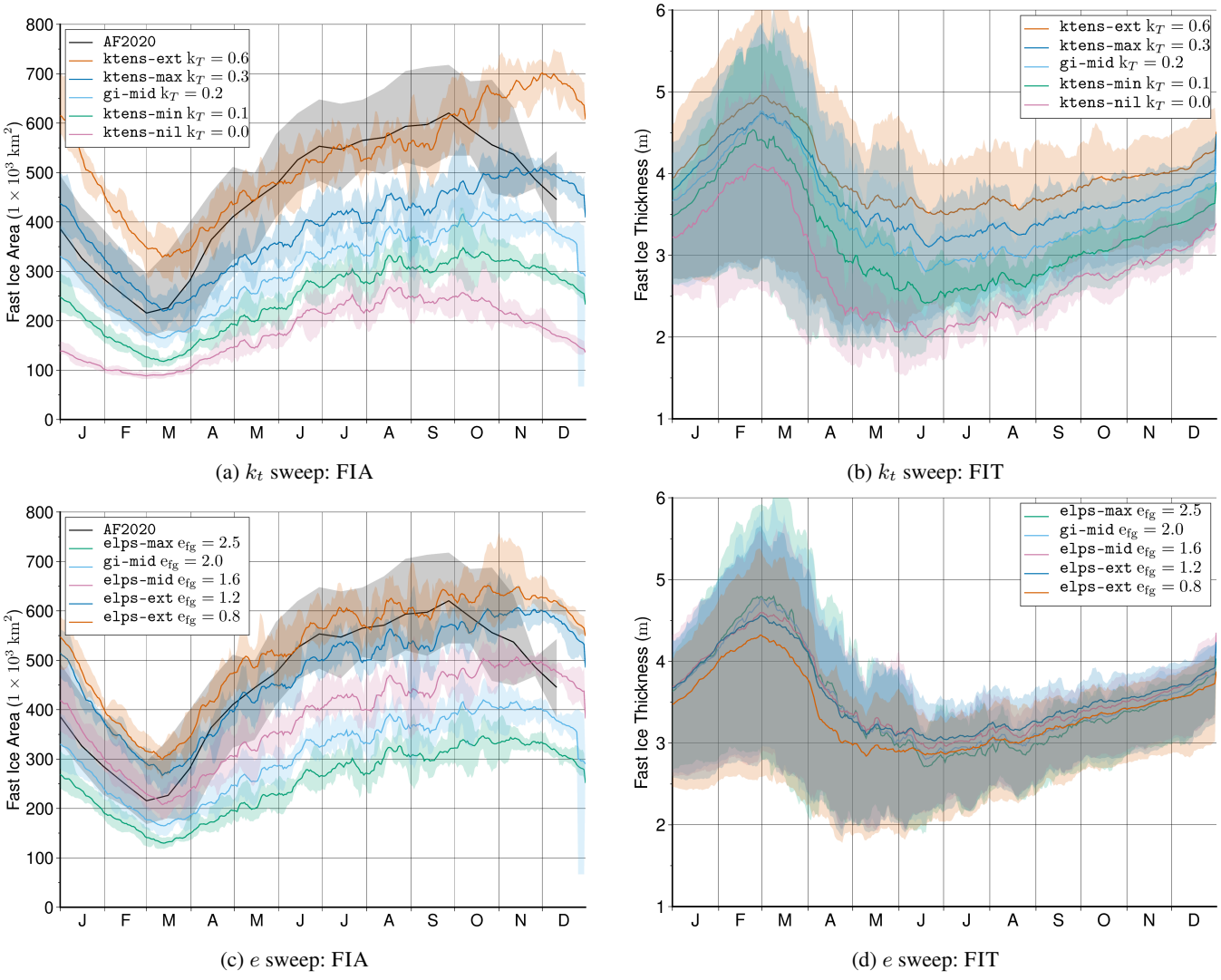

(a) k_t sweep: FIA

(b) k_t sweep: FIT

(c) e sweep: FIA

(d) e sweep: FIT

Figure C2. One–at–a–time rheology sweeps showing 1994–1999 15–day mean climatologies of circumpolar FIA and area–mean FIT over the diagnosed *binary–days* LFI mask.

C2 P^* (ice strength magnitude)

Fig. C1c–d summarises the P* sweep. P* sets the overall magnitude of internal ice strength. In panel c, increasing P* raises FIA nearly uniformly through the year—especially in winter–spring—while the phase of the seasonal cycle changes little. All members remain below the observational envelope, indicating that P* alone cannot remove the low bias in FIA relative to F2020. In panel d, very low P* coincides with unrealistically high area–mean FIT and large spread, whereas moderate values yield a more plausible range. At higher P*, LFI ice can extend into more marginal (often thinner) regions, which can reduce the area–mean FIT even if thickness in the core LFI zone changes little; seasonal timing remains broadly similar across the

https://doi.org/10.5194/egusphere-2026-1541
Preprint. Discussion started: 6 May 2026

tested range (e.g., Trivedi et al., 2025; Pirlet et al., 2025). Overall, P^* primarily modulates the *amplitude* of FIA and mitigates the excessive thickness associated with very low strength.

C3 k_t (tensile strength)

Fig. C2a–b summarises the k_T sweep. k_T controls tensile resistance (the ability to sustain sea–ice arches without tensile failure). In panel a, increasing k_T increases FIA monotonically: without tensile strength the seasonal cycle is muted, whereas moderate values ($\sim$0.2–0.3) substantially reduce the winter–spring low bias in FIA and improve peak–season behaviour. Increasing k_T further retains LFI later into spring and can overshoot the observed envelope, indicating diminishing returns and a tendency toward over–retention. Consistent with your earlier note, the diagnosed seasonal maximum also tends to shift later as tensile resistance increases.

Panel b shows that area–mean FIT generally increases with k_T. Most of the thickness change occurs from 0 up to about 0.2, with comparatively little additional change above $\sim$0.2. Notably (in contrast to the P^* sweep), k_T can increase both FIA and area–mean FIT, consistent with enhanced mechanical confinement reducing opening and export while allowing sustained thermodynamic growth (e.g., Dumont et al., 2009; Lemieux et al., 2016). A mid–range k_T value ($\sim$0.2) therefore produces most of the benefit without driving excessive retention.

C4 e (ellipse ratio / yield–curve shape)

Fig. C2c–d summarises the ellipse aspect ratio (EAR) (e) sweep. EAR controls the yield–curve shape and therefore the relative shear strength. In panel c, decreasing EAR produces a large, quasi–uniform increase in FIA and a sharper October–November peak. The intermediate case `elps-min` ($e = 1.2$) provides the closest overall match to the F2020 envelope among the experiments shown here, with improved winter growth and peak timing relative to the default member ($e = 2.0$). However, it still overshoots F2020 during late spring retreat and retains too much LFI into summer. Reducing e below unity ($e = 0.8$) yields an overly rounded yield curve and produces over–retentive LFI into summer.

In panel d, FIT is tightly constrained for $e = 1.2 - 2.5$, with only a slight reduction when $e < 1$. Lowering e produces a more rounded yield curve and increases shear strength relative to the default, favouring mechanically stable LFI configurations (Hibler, 1979; Dumont et al., 2009; Lemieux et al., 2016). The detailed balance between shear and normal deformation depends on the normal–flow rule, but the net effect here is increased persistence and delayed breakup for sufficiently low e. In practice, a reduced but not extreme eccentricity ($e \approx 1.2$) is a useful first–order tuning step toward the observed FIA climatology without resorting to unrealistically strong tensile resistance.

C5 Grounded icebergs: fraction (GIB_θ) versus placement

Fig. C3a–b shows that increasing GIB_θ (the retained fraction of GIB landmask cells) produces a stepwise, quasi–uniform rise in FIA throughout the year. Any non–zero GIB_θ substantially boosts FIA relative to the no–GIB case, while higher fractions progressively bring the seasonal cycle closer to F2020. In panel b, the thickness response is secondary: the main difference

https://doi.org/10.5194/egusphere-2026-1541
Preprint. Discussion started: 6 May 2026

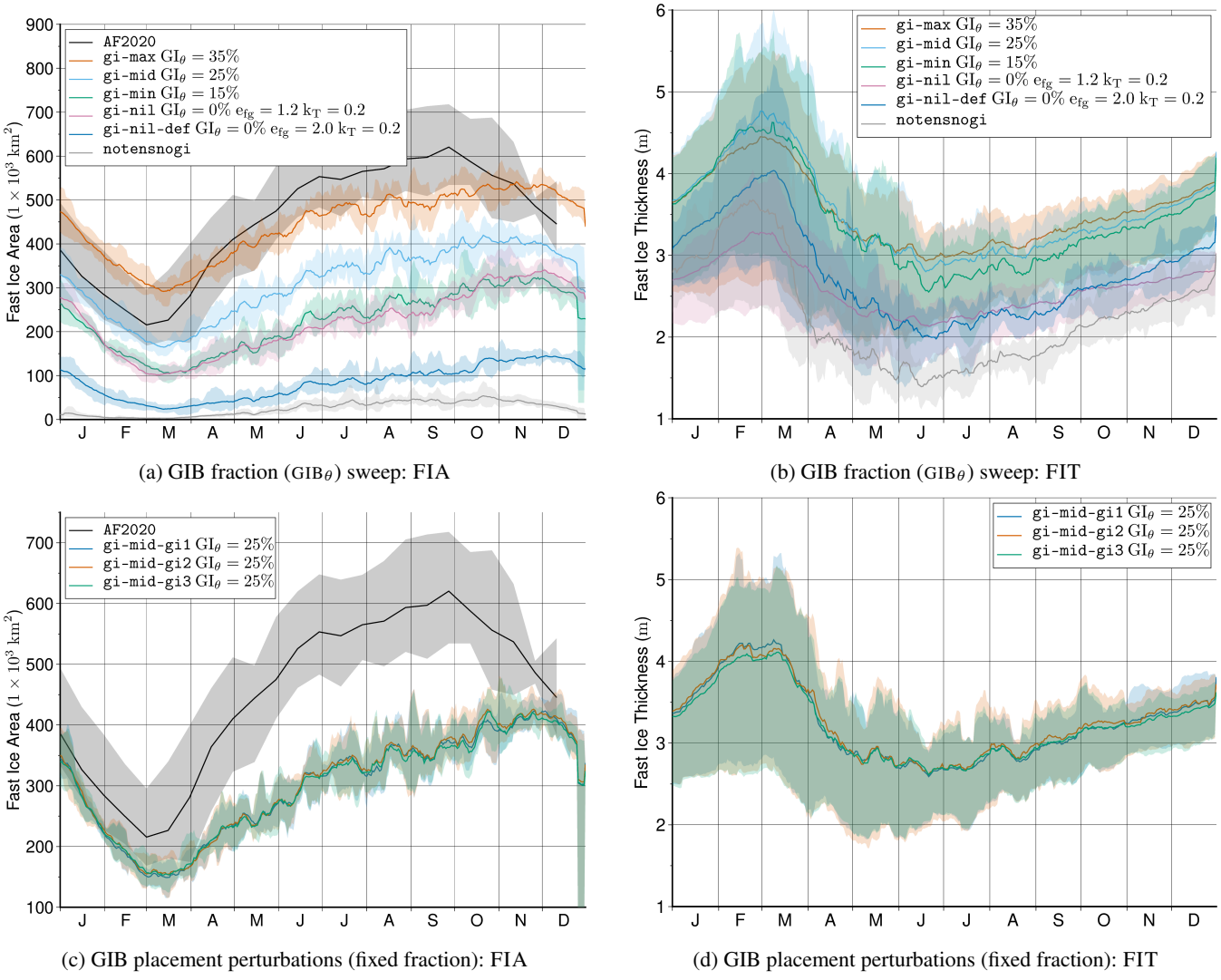

(a) GIB fraction (GIB_θ) sweep: FIA

(b) GIB fraction (GIB_θ) sweep: FIT

(c) GIB placement perturbations (fixed fraction): FIA

(d) GIB placement perturbations (fixed fraction): FIT

Figure C3. Sensitivity to grounded icebergs: (a,b) varying the retained fraction of GIB "island" cells (GIB_θ; members: 0%, 15%, 25%, 35%); (c,d) perturbing their spatial arrangement at fixed fraction.

is between no–GIB and any GIB—present member, while differences among 15–35% are modest and the timing is largely unchanged. This is consistent with the primary mechanical role of GIBs as anchoring points that suppress export and stabilise arches, affecting *area* and persistence more than local thermodynamic growth.

Fig. C3c–d shows that, at circumpolar scale and at our mask resolution, *how many* GIB cells are prescribed matters far more for domain–integrated FIA than *where* they are placed. Shuffling grounding points while holding GIB_θ fixed yields nearly identical FIA trajectories; local differences may still matter regionally (e.g., for coastal geometry and polynya structure), but these effects are second–order for the circumpolar metrics considered here.

https://doi.org/10.5194/egusphere-2026-1541
Preprint. Discussion started: 6 May 2026

Experiment	Bias (model–observation) (BIAS) $1 \times 10^3\,\mathrm{km}^2$	Pearson Correlation Coefficient (CORR)	Mean Absolute Error (MAE) $1 \times 10^3\,\mathrm{km}^2$	Root Mean Square Error (RMSE) $1 \times 10^3\,\mathrm{km}^2$
elps-min	20.4	0.849	58.8	70.4
elps-ext	71.5	0.912	72.2	89.0
elps-mid	-69.8	0.837	83.5	99.9
elps-max	-197.3	0.859	197.3	212.1
FI-heavy	158.0	0.778	158.0	177.1
ry93	-239.9	0.706	239.9	256.8
Pstar-max	-95.2	0.918	95.2	109.2
Pstar-min	-229.2	0.625	229.2	252.2
Cstar-min	-82.4	0.729	101.3	120.3
Cstar-max	-175.9	0.890	175.9	189.4
gi-max	-10.0	0.862	67.2	73.4
gi-mid	-141.6	0.865	141.6	158.6
gi-min	-227.8	0.778	227.8	243.4
gi-nil	-231.8	0.656	231.8	251.1
gi-nil-def	-368.8	0.656	368.8	383.7
notens-nogi	-426.7	0.932	426.7	441.3
ktens-max	-65.3	0.776	89.6	104.2
ktens-min	-205.6	0.923	205.6	216.7
ktens-nil	-274.2	0.979	274.2	283.6
ktens-ext	73.1	0.688	88.1	119.3
gi-mid-gi1	-151.8	0.813	151.8	170.1
gi-mid-gi2	-148.7	0.810	148.7	167.4
gi-mid-gi3	-152.6	0.807	152.6	171.5

Table D1. Circum–Antarctic LFI Area skill metrics for the full set of sensitivity experiments, evaluated against the F2020 observational product over the analysis period. Metrics include the mean signed BIAS, Pearson correlation coefficient (CORR), mean absolute error (MAE), and root–mean–square error (RMSE). Area–based statistics are reported in $1 \times 10^3\,\mathrm{km}^2$. Negative bias values denote experiments that underestimate observed fast–ice area, whereas positive values denote overestimation.

C6 Section summary

Across all sweeps, circumpolar FIA is most sensitive to k_t and e, with GIBs (GIB_θ) acting as an essential enabling constraint; by comparison, P^* and C^* primarily modulate amplitude without strongly altering phase. Changes in area–mean FIT should be interpreted cautiously because they can reflect both local thermodynamics and shifts in the diagnosed LFI footprint.

Appendix D: Table of Fast Ice Area Statistics

https://doi.org/10.5194/egusphere-2026-1541
Preprint. Discussion started: 6 May 2026

Appendix E: Table of Simulations

Table E1: Summary of `ice_diag.d` files for each simulation with the following shared non-default CICE settings: `kdyn` set to 1 (i.e., EVP enabled with `revised_evp` *enabled*), `dt` set to 1800 seconds, `ndtd` set to 1, and `ndte` set to 240 iterations per `dt`. Other significant namelist parameter settings that are consistent across all simulations are: `kterm` set to 2, `kitd` set to 1, `kstrength` set to 0 (i.e., "Hibler"), `deltaminEVP` set to 1×10^{-11}, `seabed_stress` *disabled*, `coriolis` set to "latitude", `ssh_stress` set to "geostrophic", `nprocs` set to 1232, `block_size_x` and `block_size_y` set to 20, `max_blocks` set to 10, `processor_shape` set to "square–ice", `distribution_type` set to "rake", `nx_global` set to 1440, `ny_global` set to 1080, `ns_boundary_type` set to "tripoleT", `grid_type` set to "tripole", `grid_ice` set to "B", `grid_atm` set to "A", `grid_ocn` set to "B", and `use_bathymetry` *disabled*.

Simulation Name	e	k_T	P*	C*
`Cstar-max`	2.0	0.2	27,500	**30.0**
`Cstar-min`	2.0	0.2	27,500	**10.0**
`Pstar-max`	2.0	0.2	**50,000**	20.0
`Pstar-min`	2.0	0.2	**10,000**	20.0
`elps-ext`	**0.8**	0.2	27,500	20.0
`elps-max`	**2.5**	0.2	27,500	20.0
`elps-mid`	**1.6**	0.2	27,500	20.0
`elps-min`	**1.2**	0.2	27,500	20.0
`gi-max`	2.0	0.2	27,500	20.0
`gi-mid`	2.0	0.2	27,500	20.0
`gi-mid-gi1`	2.0	0.2	27,500	20.0
`gi-mid-gi2`	2.0	0.2	27,500	20.0
`gi-mid-gi3`	2.0	0.2	27,500	20.0
`gi-min`	2.0	0.2	27,500	20.0
`gi-nil-def`	2.0	0.2	27,500	20.0
`ktens-ext`	2.0	**0.6**	27,500	20.0
`ktens-max`	2.0	**0.3**	27,500	20.0
`ktens-min`	2.0	**0.1**	27,500	20.0
`ktens-nil`	2.0	**0.0**	27,500	20.0
`notens-nogi`	2.0	**0.0**	27,500	20.0
`ry93`	2.0	0.2	27,500	20.0
`gi-nil`	**1.2**	**0.3**	**50,000**	**10.0**
`FI-heavy`	**1.2**	**0.3**	**50,000**	**10.0**

https://doi.org/10.5194/egusphere-2026-1541
Preprint. Discussion started: 6 May 2026

Competing interests. No competing interests are identified.

Author contributions. DPA conceptualised the study, carried out all model configuration and setup, experimentation, data organisation and analysis on results, drafted the manuscript (writing all text and creating all figures), and undertook all revisions. PW performed all work in relation to providing Antarctic grounded iceberg dataset. SO: advised on model configuration and setup, reviewed model results, advice on experiments, writing—review & editing. WF: review of model results, advice on experiments, supervision, writing—review & editing. PS: review of model results, advice on experiments, supervision, writing—review & editing. MP: review of model results, advice on experiments, writing—review & editing. JF: review of model results, advice on experiments, writing—review & editing. ACB: writing—review & editing of grounded iceberg satellite methodology. CA: writing—review & editing of grounded iceberg satellite methodology. ADF: Conceptualisation, methodology, writing—review & editing, supervision, project administration, funding acquisition.

Code and data availability. The version of the modified CICE source code used in this study is archived at Zenodo as *CICE_GI*, version 1.0.0, https://doi.org/10.5281/zenodo.19102795, however, this a forked version of CICE version 6.4.1 (Atwater, 2026b). The public development repository is hosted at GitHub: https://github.com/dpath2o/CICE_GI. This archive contains the forked CICE source code used for the model experiments analysed in this manuscript.

The version of the analysis and post-processing software used to generate the results and figures is archived at Zenodo as AFIM, version 1.0.0, https://doi.org/10.5281/zenodo.19102783 (Atwater, 2026a). The public development repository is hosted at GitHub: https://github.com/dpath2o/AFIM. AFIM was used for three main parts of the workflow in this study: (i) preprocessing the GIB dataset for model use, including assignment of GIB detections from the CSV dataset to the AFIM grid and application of the probabilistic thinning procedure used to generate the model GIB mask; (ii) classification of model landfast sea ice from CICE output, including the B–grid to T–grid ice–speed diagnostics and the rolling–mean and binary–day persistence methods evaluated in this paper; and (iii) post–processing and analysis of model output, including calculation of diagnostics such as FIA, FIT, and related skill metrics, together with generation of the manuscript figures and tables. The AFIM workflows used to construct the GIB mask and to classify model landfast ice are described in Appendix A and Appendix B, respectively.

The GIB dataset introduced in this study is archived at Zenodo as *Circum–Antarctic grounded iceberg dataset*, version 0.5, https://doi.org/10.5281/zenodo.19102856 (Atwater et al., 2026). The archived record includes the –CSV data file, metadata, and documentation describing the detection workflow, variable definitions, and file structure.

All DOIs cited above refer to the precise archived versions used in this manuscript.

Acknowledgements. DPA is supported in part by the Australian Defence Force through release from full-time work to work part-time (up to 8 hours per week). ADF is supported by the Australian Research Council (ARC), through grants FT230100234, LP170101090, LE220100103 and DP240100325. This project received grant funding from the Australian Government as part of the Antarctic Science Collaboration Initiative program. ADF and PW acknowledge the generous support of the Harris Charitable Trust through the Antarctic Science Foundation. PS is supported by ARC grants FT190100413, LP200100406, SR200100008, CE230100012, DP240102358, CE260100001. This research was

https://doi.org/10.5194/egusphere-2026-1541
Preprint. Discussion started: 6 May 2026

undertaken with the assistance of resources from the National Computational Infrastructure (NCI Australia), an NCRIS enabled capability supported by the Australian Government. PW is supported by the Australian Research Council's Special Research Initiative for the Antarctic Gateway Partnership (SR140300001).

https://doi.org/10.5194/egusphere-2026-1541
Preprint. Discussion started: 6 May 2026

References

Abram, N. J., Purich, A., England, M. H., McCormack, F. S., Strugnell, J. M., Bergstrom, D. M., Vance, T. R., Stål, T., Wienecke, B., Heil, P., Doddridge, E. W., Sallée, J.-B., Williams, T. J., Reading, A. M., Mackintosh, A., Reese, R., Winkelmann, R., Klose, A. K., Boyd, P. W., Chown, S. L., and Robinson, S. A.: Emerging Evidence of Abrupt Changes in the Antarctic Environment, Nature, 644, 621–633, https://doi.org/10.1038/s41586-025-09349-5, 2025.

Ainley, D. G., Larue, M. A., Stirling, I., Stammerjohn, S., and Siniff, D. B.: An Apparent Population Decrease, or Change in Distribution, of Weddell Seals along the Victoria Land Coast, Marine Mammal Science, 31, 1338–1361, https://doi.org/10.1111/mms.12220, 2015.

Atwater, D. P.: AFIM: Antarctic Fast Ice Modelling analysis software, https://doi.org/10.5281/zenodo.19102783, 2026a.

Atwater, D. P.: CICE_GI: Modified CICE source code for Antarctic fast-ice simulations, https://doi.org/10.5281/zenodo.19102795, 2026b.

Atwater, D. P., Wongpan, P., and Fraser, A. D.: Circum-Antarctic grounded iceberg dataset, https://doi.org/10.5281/zenodo.19102856, 2026.

Bouchat, A. and Tremblay, B.: Using Sea-Ice Deformation Fields to Constrain the Mechanical Strength Parameters of Geophysical Sea Ice, Journal of Geophysical Research: Oceans, 122, 5802–5825, https://doi.org/10.1002/2017JC013020, 2017.

Bouchat, A., Hutter, N., Chanut, J., Dupont, F., Dukhovskoy, D., Garric, G., Lee, Y. J., Lemieux, J.-F., Lique, C., Losch, M., Maslowski, W., Myers, P. G., Ólason, E., Rampal, P., Rasmussen, T., Talandier, C., Tremblay, B., and Wang, Q.: Sea Ice Rheology Experiment (SIREx): 1. Scaling and Statistical Properties of Sea-Ice Deformation Fields, Journal of Geophysical Research: Oceans, 127, e2021JC017 667, https://doi.org/10.1029/2021JC017667, 2022.

Bouillon, S., Fichefet, T., Legat, V., and Madec, G.: The Elastic–Viscous–Plastic Method Revisited, Ocean Modelling, 71, 2–12, https://doi.org/10.1016/j.ocemod.2013.05.013, 2013.

Cougnon, E. A., Galton-Fenzi, B. K., Meijers, A. J. S., and Legrésy, B.: Modeling Interannual Dense Shelf Water Export in the Region of the Mertz Glacier Tongue (1992–2007), Journal of Geophysical Research: Oceans, 118, 5858–5872, https://doi.org/10.1002/2013JC008790, 2013.

Cougnon, E. A., Galton-Fenzi, B. K., Rintoul, S. R., Legrésy, B., Williams, G. D., Fraser, A. D., and Hunter, J. R.: Regional Changes in Icescape Impact Shelf Circulation and Basal Melting, Geophysical Research Letters, 44, 11,519–11,527, https://doi.org/10.1002/2017GL074943, 2017.

Crocker, G. B. and Wadhams, P.: Breakup of Antarctic Fast Ice, Cold Regions Science and Technology, 17, 61–76, https://doi.org/10.1016/S0165-232X(89)80016-3, 1989.

Day, N. S., Bennetts, L. G., O'Farrell, S. P., Alberello, A., and Montiel, F.: Analysis of the Antarctic Marginal Ice Zone Based on Unsupervised Classification of Standalone Sea Ice Model Data, Journal of Geophysical Research: Oceans, 129, e2024JC020 953, https://doi.org/10.1029/2024JC020953, 2024.

Dumont, D., Gratton, Y., and Arbetter, T. E.: Modeling the Dynamics of the North Water Polynya Ice Bridge, Journal of Physical Oceanography, 39, 1448–1461, https://doi.org/10.1175/2008JPO3965.1, 2009.

EUMETSAT: Global Sea Ice Drift Climate Data Record Release v1.0, EUMETSAT Data Store, 2025.

Fraser, A. D., Ohshima, K. I., Nihashi, S., Massom, R. A., Tamura, T., Nakata, K., Williams, G. D., Carpentier, S., and Willmes, S.: Landfast Ice Controls on Sea-Ice Production in the Cape Darnley Polynya: A Case Study, Remote Sensing of Environment, 233, 111 315, https://doi.org/10.1016/j.rse.2019.111315, 2019.

https://doi.org/10.5194/egusphere-2026-1541
Preprint. Discussion started: 6 May 2026

Fraser, A. D., Massom, R. A., Ohshima, K. I., Willmes, S., Kappes, P. J., Cartwright, J., and Porter-Smith, R.: High-Resolution Mapping of Circum-Antarctic Landfast Sea Ice Distribution, 2000–2018, Earth System Science Data, 12, 2987–2999, https://doi.org/10.5194/essd-12-2987-2020, 2020.

Fraser, A. D., Massom, R. A., Handcock, M. S., Reid, P., Ohshima, K. I., Raphael, M. N., Cartwright, J., Klekociuk, A. R., Wang, Z., and Porter-Smith, R.: Eighteen-Year Record of Circum-Antarctic Landfast-Sea-Ice Distribution Allows Detailed Baseline Characterisation and Reveals Trends and Variability, The Cryosphere, 15, 5061–5077, https://doi.org/10.5194/tc-15-5061-2021, 2021.

Fraser, A. D., Wongpan, P., Langhorne, P. J., Klekociuk, A. R., Kusahara, K., Lannuzel, D., Massom, R. A., Meiners, K. M., Swadling, K. M., Atwater, D. P., Brett, G. M., Corkill, M., Dalman, L. A., Fiddes, S., Granata, A., Guglielmo, L., Heil, P., Leonard, G. H., Mahoney, A. R., McMinn, A., van der Merwe, P., Weldrick, C. K., and Wienecke, B.: Antarctic Landfast Sea Ice: A Review of Its Physics, Biogeochemistry and Ecology, Reviews of Geophysics, 61, e2022RG000 770, https://doi.org/10.1029/2022RG000770, 2023.

Fraser, A. D., Day, N., Wang, Z., Bennetts, L. G., Liu, Q., O'Farrell, S., Coleman, R., Voermans, J., Xu, S., Zhu, W., Auger, M., Massom, R. A., Wongpan, P., Craw, L., Brouwer, J., Toyota, T., Heil, P., and Horvat, C.: Revealing the Antarctic Marginal Ice Zone: A Decade-Long Wave-in-Ice Climatology, Nature Communications, 2025.

GAMMA Remote Sensing AG: GAMMA Software, 2024.

Giles, A., Massom, R., and Lytle, V.: Fast-Ice Distribution in East Antarctica during 1997 and 1999 Determined Using RADARSAT Data, Journal of Geophysical Research (Oceans), 113, https://doi.org/10.1029/2007JC004139, 2008.

Gomez-Fell, R., Rack, W., Purdie, H., and Marsh, O.: Parker Ice Tongue Collapse, Antarctica, Triggered by Loss of Stabilizing Land-Fast Sea Ice, Geophysical Research Letters, 49, e2021GL096 156, https://doi.org/10.1029/2021GL096156, 2022.

Gwyther, D. E., Galton-Fenzi, B. K., Hunter, J. R., and Roberts, J. L.: Simulated Melt Rates for the Totten and Dalton Ice Shelves, Ocean Science, 10, 267–279, https://doi.org/10.5194/os-10-267-2014, 2014.

Hendricks, S., Paul, S., and Rinne, E.: ESA Sea Ice Climate Change Initiative (Sea_ice_cci): Southern Hemisphere Sea Ice Thickness (L3C), v2.0, https://doi.org/10.5285/B1F1AC03077B4AA784C5A413A2210BF5, 2024.

Henley, S. F., Cozzi, S., Fripiat, F., Lannuzel, D., Nomura, D., Thomas, D. N., Meiners, K. M., Vancoppenolle, M., Arrigo, K., Stefels, J., van Leeuwe, M., Moreau, S., Jones, E. M., Fransson, A., Chierici, M., and Delille, B.: Macronutrient Biogeochemistry in Antarctic Land-Fast Sea Ice: Insights from a Circumpolar Data Compilation, Marine Chemistry, 257, 104 324, https://doi.org/10.1016/j.marchem.2023.104324, 2023.

Hersbach, H., Bell, B., Berrisford, P., Hirahara, S., Horányi, A., Muñoz-Sabater, J., Nicolas, J., Peubey, C., Radu, R., Schepers, D., Simmons, A., Soci, C., Abdalla, S., Abellan, X., Balsamo, G., Bechtold, P., Biavati, G., Bidlot, J., Bonavita, M., De Chiara, G., Dahlgren, P., Dee, D., Diamantakis, M., Dragani, R., Flemming, J., Forbes, R., Fuentes, M., Geer, A., Haimberger, L., Healy, S., Hogan, R. J., Hólm, E., Janisková, M., Keeley, S., Laloyaux, P., Lopez, P., Lupu, C., Radnoti, G., de Rosnay, P., Rozum, I., Vamborg, F., Villaume, S., and Thèpaut, J.-N.: The ERA5 Global Reanalysis, Quarterly Journal of the Royal Meteorological Society, 146, 1999–2049, https://doi.org/10.1002/qj.3803, 2020.

Hibler, W. D.: A Dynamic Thermodynamic Sea Ice Model, Journal of Physical Oceanography, 9, 815–846, https://doi.org/10.1175/1520-0485(1979)009<0815:ADTSIM>2.0.CO;2, 1979.

Hill, C., DeLuca, C., Balaji, V., Suarez, M., and da Silva, A.: The Earth System Modeling Framework, Computing in Science & Engineering, 6, 18–28, 2004.

Hunke, E. C.: Viscous–Plastic Sea Ice Dynamics with the EVP Model: Linearization Issues, Journal of Computational Physics, 170, 18–38, https://doi.org/10.1006/jcph.2001.6710, 2001.

https://doi.org/10.5194/egusphere-2026-1541
Preprint. Discussion started: 6 May 2026

Hunke, E. C. and Dukowicz, J. K.: An Elastic–Viscous–Plastic Model for Sea Ice Dynamics, Journal of Physical Oceanography, 27, 1849–1867, https://doi.org/10.1175/1520-0485(1997)027<1849:AEVPMF>2.0.CO;2, 1997.

Hunke, E. C., DuVivier, A., et al.: CICE User's Guide: Los Alamos Sea Ice Model (CICE) Version 6.4.1, 2022.

Huot, P.-V., Kittel, C., Fichefet, T., Jourdain, N. C., Sterlin, J., and Fettweis, X.: Effects of the Atmospheric Forcing Resolution on Simulated Sea Ice and Polynyas off Adélie Land, East Antarctica, Ocean Modelling, 168, 101 901, https://doi.org/10.1016/j.ocemod.2021.101901, 2021.

Hutter, N., Bouchat, A., Dupont, F., Dukhovskoy, D., Koldunov, N., Lee, Y. J., Lemieux, J.-F., Lique, C., Losch, M., Maslowski, W., Myers, P. G., Ólason, E., Rampal, P., Rasmussen, T., Talandier, C., Tremblay, B., and Wang, Q.: Sea Ice Rheology Experiment (SIREx): 2. Evaluating Linear Kinematic Features in High-Resolution Sea Ice Simulations, Journal of Geophysical Research: Oceans, 127, e2021JC017 666, https://doi.org/10.1029/2021JC017666, 2022.

Inall, M. E., Brearley, J. A., Henley, S. F., Fraser, A. D., and Reed, S.: Landfast Ice Controls on Turbulence in Antarctic Coastal Seas, Journal of Geophysical Research: Oceans, 127, e2021JC017 963, https://doi.org/10.1029/2021JC017963, 2022.

Jezek, K., Curlander, J., Carsey, F., Wales, C., and Barry, R.: RAMP AMM-1 SAR Image Mosaic of Antarctica, Version 2, 2013.

Johnson, G. C.: Quantifying Antarctic Bottom Water and North Atlantic Deep Water Volumes, Journal of Geophysical Research: Oceans, 113, https://doi.org/10.1029/2007JC004477, 2008.

Kimmritz, M., Danilov, S., and Losch, M.: The Adaptive EVP Method for Solving the Sea Ice Momentum Equation, Ocean Modelling, 101, 59–67, https://doi.org/10.1016/j.ocemod.2016.03.004, 2016.

Kiss, A. E., Hogg, A. M., Hannah, N., Boeira Dias, F., Brassington, G. B., Chamberlain, M. A., Chapman, C., Dobrohotoff, P., Domingues, C. M., Duran, E. R., England, M. H., Fiedler, R., Griffies, S. M., Heerdegen, A., Heil, P., Holmes, R. M., Klocker, A., Marsland, S. J., Morrison, A. K., Munroe, J., Nikurashin, M., Oke, P. R., Pilo, G. S., Richet, O., Savita, A., Spence, P., Stewart, K. D., Ward, M. L., Wu, F., and Zhang, X.: ACCESS-OM2 v1.0: A Global Ocean–Sea Ice Model at Three Resolutions, Geoscientific Model Development, 13, 401–442, https://doi.org/10.5194/gmd-13-401-2020, 2020.

König-Beatty, C. and Holland, D. M.: Modeling Landfast Sea Ice by Adding Tensile Strength, Journal of Physical Oceanography, 40, 185–198, https://doi.org/10.1175/2009JPO4105.1, 2010.

Kusahara, K., Hasumi, H., and Tamura, T.: Modeling Sea Ice Production and Dense Shelf Water Formation in Coastal Polynyas around East Antarctica, Journal of Geophysical Research: Oceans, 115, https://doi.org/10.1029/2010JC006133, 2010.

Kusahara, K., Hasumi, H., Fraser, A. D., Aoki, S., Shimada, K., Williams, G. D., Massom, R., and Tamura, T.: Modeling Ocean–Cryosphere Interactions off Adélie and George V Land, East Antarctica, Journal of Climate, 30, 163–188, https://doi.org/10.1175/JCLI-D-15-0808.1, 2017a.

Kusahara, K., Williams, G. D., Tamura, T., Massom, R., and Hasumi, H.: Dense Shelf Water Spreading from Antarctic Coastal Polynyas to the Deep Southern Ocean: A Regional Circumpolar Model Study, Journal of Geophysical Research: Oceans, 122, 6238–6253, https://doi.org/10.1002/2017JC012911, 2017b.

Labrousse, S., Fraser, A. D., Sumner, M., Le Manach, F., Sauser, C., Horstmann, I., Devane, E., Delord, K., Jenouvrier, S., and Barbraud, C.: Landfast Ice: A Major Driver of Reproductive Success in a Polar Seabird, Biology Letters, 17, 20210 097, https://doi.org/10.1098/rsbl.2021.0097, 2021.

Lange, K. A., Bradley, A. C., Duncan, K., and Farrell, S. L.: Grounded Ridge Detection and Characterization along the Alaska Arctic Coastline Using ICESat-2 Surface Height Retrievals, The Cryosphere, 19, 2045–2065, https://doi.org/10.5194/tc-19-2045-2025, 2025.

Leane, E. and Maddison, B.: A Biography of Iceberg B09B, Australian Humanities Review, pp. 99–115, 2018.

https://doi.org/10.5194/egusphere-2026-1541
Preprint. Discussion started: 6 May 2026

Lemieux, J.-F., Tremblay, L. B., Dupont, F., Plante, M., Smith, G. C., and Dumont, D.: A Basal Stress Parameterization for Modeling Landfast Ice, Journal of Geophysical Research: Oceans, 120, 3157–3173, https://doi.org/10.1002/2014JC010678, 2015.

Lemieux, J.-F., Dupont, F., Blain, P., Roy, F., Smith, G. C., and Flato, G. M.: Improving the Simulation of Landfast Ice by Combining Tensile Strength and a Parameterization for Grounded Ridges, Journal of Geophysical Research: Oceans, 121, 7354–7368, https://doi.org/10.1002/2016JC012006, 2016.

Lemieux, J.-F., Lei, J., Dupont, F., Roy, F., Losch, M., Lique, C., and Laliberté, F.: The Impact of Tides on Simulated Landfast Ice in a Pan-Arctic Ice-Ocean Model, Journal of Geophysical Research: Oceans, 123, 7747–7762, https://doi.org/10.1029/2018JC014080, 2018.

Li, X., Shokr, M., Hui, F., Chi, Z., Heil, P., Chen, Z., Yu, Y., Zhai, M., and Cheng, X.: The Spatio-Temporal Patterns of Landfast Ice in Antarctica during 2006–2011 and 2016–2017 Using High-Resolution SAR Imagery, Remote Sensing of Environment, 242, 111 736, https://doi.org/10.1016/j.rse.2020.111736, 2020a.

Li, Z., Zhao, J., Su, J., Li, C., Cheng, B., Hui, F., Yang, Q., and Shi, L.: Spatial and Temporal Variations in the Extent and Thickness of Arctic Landfast Ice, Remote Sensing, 12, 64, https://doi.org/10.3390/rs12010064, 2020b.

Liang, J., Pitt, J. P. A., and Bennetts, L. G.: Pan-Antarctic Assessment of Ice Shelf Flexural Responses to Ocean Waves, Journal of Geophysical Research: Oceans, 129, e2023JC020 824, https://doi.org/10.1029/2023JC020824, 2024.

Lieser, J. L.: A Numerical Model for Short-Term Sea Ice Forecasting in the Arctic, Ph.D. thesis, Universitaet Bremen, 2004.

Liu, Y., Losch, M., Hutter, N., and Mu, L.: A New Parameterization of Coastal Drag to Simulate Landfast Ice in Deep Marginal Seas in the Arctic, Journal of Geophysical Research: Oceans, 127, e2022JC018 413, https://doi.org/10.1029/2022JC018413, 2022.

Mahoney, A., Eicken, H., Gaylord, A. G., and Shapiro, L.: Alaska Landfast Sea Ice: Links with Bathymetry and Atmospheric Circulation, Journal of Geophysical Research, 112, C02 001, https://doi.org/10.1029/2006JC003559, 2007a.

Mahoney, A., Eicken, H., and Shapiro, L.: How Fast Is Landfast Sea Ice? A Study of the Attachment and Detachment of Nearshore Ice at Barrow, Alaska, Cold Regions Science and Technology, 47, 233–255, https://doi.org/10.1016/j.coldregions.2006.09.005, 2007b.

Mahoney, A. R., Eicken, H., Gaylord, A. G., and Gens, R.: Landfast Sea Ice Extent in the Chukchi and Beaufort Seas: The Annual Cycle and Decadal Variability, Cold Regions Science and Technology, 103, 41–56, https://doi.org/10.1016/j.coldregions.2014.03.003, 2014.

Maksym, T., Stammerjohn, S. E., Ackley, S., and Massom, R.: Antarctic Sea Ice—A Polar Opposite?, Oceanography, 25, 140–151, https://doi.org/10.5670/oceanog.2012.88, 2012.

Massom, R., Scambos, T., Bennetts, L., Reid, P., Squire, V., and Stammerjohn, S.: Antarctic Ice Shelf Disintegration Triggered by Sea Ice Loss and Ocean Swell, Nature, 558, https://doi.org/10.1038/s41586-018-0212-1, 2018.

Massom, R. A., Harris, P., Michael, K. J., and Potter, M.: The Distribution and Formative Processes of Latent-Heat Polynyas in East Antarctica, Annals of Glaciology, 27, 420–426, https://doi.org/10.3189/1998AoG27-1-420-426, 1998.

Massom, R. A., Hill, K. L., Lytle, V. I., Worby, A. P., Paget, M., and Allison, I.: Effects of Regional Fast-Ice and Iceberg Distributions on the Behaviour of the Mertz Glacier Polynya, East Antarctica, Annals of Glaciology, 33, 391–398, https://doi.org/10.3189/172756401781818518, 2001.

Massom, R. A., Giles, A. B., Warner, R. C., Fricker, H. A., Legrésy, B., Hyland, G., Lescarmontier, L., and Young, N.: External Influences on the Mertz Glacier Tongue (East Antarctica) in the Decade Leading up to Its Calving in 2010, Journal of Geophysical Research: Earth Surface, 120, 490–506, https://doi.org/10.1002/2014JF003223, 2015.

Meier, W., Peng, G., Scott, D., Savoie, M., Armstrong, R., Knowles, K., and Richardson, A.: NOAA/NSIDC Climate Data Record of Passive Microwave Sea Ice Concentration, Version 4, https://doi.org/10.7265/efmz-2t65, 2021.

https://doi.org/10.5194/egusphere-2026-1541
Preprint. Discussion started: 6 May 2026

Morales Maqueda, M. A., Willmott, A. J., and Biggs, N. R. T.: Polynya Dynamics: A Review of Observations and Modeling, Reviews of Geophysics, 42, https://doi.org/10.1029/2002RG000116, 2004.

Murray, R. J.: Explicit Generation of Orthogonal Grids for Ocean Models, Journal of Computational Physics, 126, 251–273, https://doi.org/10.1006/jcph.1996.0136, 1996.

Nakayama, Y., Ohshima, K. I., Matsumura, Y., Fukamachi, Y., and Hasumi, H.: A Numerical Investigation of Formation and Variability of Antarctic Bottom Water off Cape Darnley, East Antarctica, Journal of Physical Oceanography, 44, 2921–2937, https://doi.org/10.1175/JPO-D-14-0069.1, 2014.

Nihashi, S. and Ohshima, K. I.: Circumpolar Mapping of Antarctic Coastal Polynyas and Landfast Sea Ice: Relationship and Variability, Journal of Climate, 28, 3650–3670, https://doi.org/10.1175/JCLI-D-14-00369.1, 2015.

Ochwat, N. E., Scambos, T. A., Banwell, A. F., Anderson, R. S., Maclennan, M. L., Picard, G., Shates, J. A., Marinsek, S., Margonari, L., Truffer, M., and Pettit, E. C.: Triggers of the 2022 Larsen B Multi-Year Landfast Sea Ice Breakout and Initial Glacier Response, The Cryosphere, 18, 1709–1731, https://doi.org/10.5194/tc-18-1709-2024, 2024.

Olason, E.: A Dynamical Model of Kara Sea Land-Fast Ice, Journal of Geophysical Research: Oceans, 121, 3141–3158, https://doi.org/10.1002/2016JC011638, 2016.

Orsi, A. H., Jacobs, S. S., Gordon, A. L., and Visbeck, M.: Cooling and Ventilating the Abyssal Ocean, Geophysical Research Letters, 28, 2923–2926, https://doi.org/10.1029/2001GL012830, 2001.

Panteleev, G., Yaremchuk, M., Stroh, J. N., Francis, O. P., and Allard, R.: Parameter Optimization in Sea Ice Models with Elastic–Viscoplastic Rheology, The Cryosphere, 14, 4427–4451, https://doi.org/10.5194/tc-14-4427-2020, 2020.

Pauling, A. G., Bitz, C. M., Smith, I. J., and Langhorne, P. J.: The Response of the Southern Ocean and Antarctic Sea Ice to Freshwater from Ice Shelves in an Earth System Model, Journal of Climate, 29, 1655–1672, https://doi.org/10.1175/JCLI-D-15-0501.1, 2016.

Pellichero, V., Sallée, J.-B., Schmidtko, S., Roquet, F., and Charrassin, J.-B.: The Ocean Mixed Layer under Southern Ocean Sea-Ice: Seasonal Cycle and Forcing, Journal of Geophysical Research: Oceans, 122, 1608–1633, https://doi.org/10.1002/2016JC011970, 2017.

Petty, A. A., Holland, P. R., and Feltham, D. L.: Sea Ice and the Ocean Mixed Layer over the Antarctic Shelf Seas, The Cryosphere, 8, 761–783, https://doi.org/10.5194/tc-8-761-2014, 2014.

Pirlet, N., Fichefet, T., Vancoppenolle, M., de Lavergne, C., and Jourdain, N.: Effects of a Landfast Ice Representation on Antarctic Shelf Water Properties and Ice Shelf Melt Simulated by NEMO4-SI^3, https://doi.org/10.22541/essoar.176218943.36540527/v1, 2025.

Porter-Smith, R., McKinlay, J., Fraser, A., and Massom, R.: Coastal Complexity of the Antarctic Continent, Earth System Science Data, 13, 3103–3114, https://doi.org/10.5194/essd-13-3103-2021, 2021.

Tamura, T., Williams, G. D., Fraser, A. D., and Ohshima, K. I.: Potential Regime Shift in Decreased Sea Ice Production after the Mertz Glacier Calving, Nature Communications, 3, 826, https://doi.org/10.1038/ncomms1820, 2012.

Tamura, T., Ohshima, K. I., Fraser, A. D., and Williams, G. D.: Sea Ice Production Variability in Antarctic Coastal Polynyas, Journal of Geophysical Research: Oceans, 121, 2967–2979, https://doi.org/https://doi.orpppg/10.1002/2015JC011537, 2016.

Teder, N. J., Bennetts, L. G., Reid, P. A., and Massom, R. A.: Sea Ice-Free Corridors for Large Swell to Reach Antarctic Ice Shelves, Environmental Research Letters, 17, 045 026, https://doi.org/10.1088/1748-9326/ac5edd, 2022.

Teder, N. J., Bennetts, L. G., Reid, P. A., Massom, R. A., Pitt, J. P. A., Scambos, T. A., and Fraser, A. D.: Large-Scale Ice-Shelf Calving Events Follow Prolonged Amplifications in Flexure, Nature Geoscience, 18, 599–606, https://doi.org/10.1038/s41561-025-01713-4, 2025.

Toyota, T. and Kimura, N.: An Examination of the Sea Ice Rheology for Seasonal Ice Zones Based on Ice Drift and Thickness Observations, Journal of Geophysical Research: Oceans, 123, 1406–1428, https://doi.org/10.1002/2017JC013627, 2018.

https://doi.org/10.5194/egusphere-2026-1541
Preprint. Discussion started: 6 May 2026

Tremblay, L.-B. and Hakakian, M.: Estimating the Sea Ice Compressive Strength from Satellite-Derived Sea Ice Drift and NCEP Reanalysis Data, Journal of Physical Oceanography, 36, 2165–2172, https://doi.org/10.1175/JPO2954.1, 2006.

Trivedi, S., Hobbs, W. R., and Raphael, M.: An Assessment of Antarctic Sea-ice Thickness in CMIP6 Simulations with Comparison to the Satellite-based Observations and Reanalyses, EGUsphere, pp. 1–28, https://doi.org/10.5194/egusphere-2024-2744, 2025.

Truckenbrodt, J., Cremer, F., Baris, I., and Eberle, J.: pyroSAR — a Framework for Large-Scale SAR Satellite Data Processing, in: Proceedings of the Big Data from Space Conference (BiDS), pp. 19–20, Munich, Germany, 2019.

Ungermann, M., Tremblay, L. B., Martin, T., and Losch, M.: Impact of the Ice Strength Formulation on the Performance of a Sea Ice Thickness Distribution Model in the Arctic, Journal of Geophysical Research: Oceans, 122, 2090–2107, https://doi.org/10.1002/2016JC012128, 2017.

Van Achter, G., Fichefet, T., Goosse, H., Pelletier, C., Sterlin, J., Huot, P.-V., Lemieux, J.-F., Fraser, A. D., Haubner, K., and Porter-Smith, R.: Modelling Landfast Sea Ice and Its Influence on Ocean–Ice Interactions in the Area of the Totten Glacier, East Antarctica, Ocean Modelling, 169, 101 920, https://doi.org/10.1016/j.ocemod.2021.101920, 2022.

Vancoppenolle, M., Jourdain, N. C., Fichefet, T., Fraser, A. D., Massonnet, F., Mathiot, P., Madec, G., Mehlmann, C., Olivé Abelló, A., Atwater, D. P., et al.: Why Icebergs and Their Interactions with Sea Ice Should Be Included in Earth System Models?, 2025.

Wongpan, P., Meiners, K. M., Vancoppenolle, M., Fraser, A. D., Moreau, S., Saenz, B. T., Swadling, K. M., and Lannuzel, D.: Gross Primary Production of Antarctic Landfast Sea Ice: A Model-Based Estimate, Journal of Geophysical Research: Oceans, 129, e2024JC021 348, https://doi.org/10.1029/2024JC021348, 2024.

Wongpan, P., Corkill, M., Macfarlane, A. R., Dalman, L. A., and Fraser, A. D.: Sea Ice Properties: An Ice-Type Perspective, in: Comprehensive Cryospheric Science and Environmental Change, p. in press, Elsevier, https://doi.org/10.1016/B978-0-323-85242-5.00035-X, 2025.

Wright, C. S. and Priestly, R. E.: British (Terra Nova) Antarctic Expedition: Glaciology, Tech. rep., Captain Scott Antarctic Fund, London, 1922.

Xia, Y., Gwyther, D. E., Galton-Fenzi, B., Cougnon, E. A., Fraser, A. D., and Moore, J. C.: Eddy and Tidal Driven Basal Melting of the Totten and Moscow University Ice Shelves, Frontiers in Marine Science, 10, https://doi.org/10.3389/fmars.2023.1159353, 2023.

Zhuang, J., Branstetter, M., Singh, B., Rasch, P. J., Xie, S., Tesfa, T., and Tang, Q.: xESMF: Universal Regridder for Geospatial Data, Journal of Open Source Software, 6, 3167, https://doi.org/10.21105/joss.03167, 2021.

Zuo, H., Balmaseda, M. A., Tietsche, S., Mogensen, K., and Mayer, M.: The ECMWF Operational Ensemble Reanalysis System ORAS5, Climate Dynamics, 52, 1435–1463, https://doi.org/10.1007/s00382-018-4231-7, 2019.